Lineage domains and cytoskeletal cables organize a cellular square grid in a crustacean

Beatrice L. Steinert[1,2,3], Leo Blondel[4,5], Chandrashekar Kuyyamudi[1,6], Evangelia Stamataki[7,8], Anastasios Pavlopoulos[7,8], Cassandra G. Extavour[1,4,6 *]

1 Department of Organismic and Evolutionary Biology, Harvard University
2 Department of the History of Science, Harvard University
2 Current address: Brown University
3 Department of Molecular and Cellular Biology, Harvard University
4 Current address: Learning Planet Institute, France
6 Howard Hughes Medical Institute
7 Janelia Research Campus, Howard Hughes Medical Institute
8 Current address: Institute of Molecular Biology and Biotechnology FORTH, Greece

* Correspondence: extavour@oeb.harvard.edu

Abstract

To build tissues, and ultimately functional bodies, cells in early embryos must arrange into specific patterns. In most animals, epithelial tissues exhibit a predominantly hexagonal space-packing geometry. However, in many species of the largest group of crustaceans, the Malacostraca, the embryonic epithelium takes on the striking form of a grid made up of predominantly square cells, sequential rows of which establish the adult segmented body plan. After square cells emerge, their organization appears to be maintained by specific cell division patterns. However, the mechanisms that initially generate square cells from hexagonal precursors are unknown. Here we address this problem by combining long-term multiview lightsheet microscopy, immunohistochemistry, laser ablation, and pharmacological perturbation. We show that in the emerging model crustacean *Parhyale hawaiensis* this highly unusual grid geometry is first initiated from two perpendicular axes that are established sequentially according to different cellular mechanisms. The first axis arises dorso-ventrally at a tensile lineage compartment boundary, while the second emerges at the ventral midline through lineage-independent cell intercalation driven by tensile actomyosin cables. We show that these midline cables are necessary for organizing square-cell packing as well as for proper expression of the segmentation gene *engrailed*. Our findings show that both cell lineage-specific behaviors, as well as lineage-independent supracellular structures, are required to establish square grid epithelial organization and a segmented body plan.

Keywords: amphipod, *Parhyale hawaiensis*, ectoderm, segmentation, epithelium, morphogenesis

41 # Introduction

42

43 The organization of cells and tissues during development is fundamental for multicellular
44 organisms. During embryogenesis, cells must be shaped at both the individual and collective tissue
45 levels to form functional structures at every stage of ontogeny. It has been appreciated since the
46 late nineteenth century that mechanical forces and geometric properties of cells and tissues play a
47 central role in morphogenesis, the generation of form during development[1]. Despite the
48 predominant focus on the role of genes in tissue patterning during the last half century[2–5], recent
49 decades have witnessed a resurgence of interest in the mechanics of development at the cell and
50 tissue scales of biological organization[6–8]. Harnessing techniques for live imaging and
51 computational image processing and annotation, recent work has begun to couple mechanical and
52 genetic contributions to tissue organization during embryogenesis[9]. However, these investigations
53 have been largely limited to a small number of model laboratory organisms, most of which are
54 vertebrates, giving us a narrow phylogenetic sampling.

55 The arthropods, which include insects and crustaceans, are and always have been the most
56 speciose group of animals on earth[10]. All arthropods have segmented body plans that are
57 established early in embryonic development[11]. Segmentation is evident in embryonic ectodermal
58 epithelia[12], tissues in which cells are tightly adhered to one another in a monolayer sheet and apical
59 cell faces form a confluent network of polygons[13]. Most epithelia that have been studied to date
60 are those in which constituent cells exhibit predominantly hexagonal packing with three-way
61 vertices, which is the geometry with minimal surface energy and maximal space-filling
62 efficiency[14–18]. During segmentation in the fruit fly *Drosophila melanogaster*[19,20] and the
63 milkweed bug *Oncopeltus fasciatus*[21], a small number of cells at segment boundaries briefly stray

64 from this geometry to give rise to an increased number of 4-way vertices, suggesting an altered
65 mechanical state. However, most epithelial cells retain their hexagonal shapes throughout
66 segmentation and early morphogenesis[22–24]. In *D. melanogaster*, maintaining boundaries between
67 embryonic segments requires tensile cables of actin and non-muscle myosin (myosin 2), which are
68 mechanically coupled across the tissue and prevent cell mixing across the boundary[19,24].

69 In contrast, in the early embryonic ectodermal epithelium of malacostracan crustaceans
70 (including shrimp, lobsters, isopods and amphipods) cells are packed into a grid of square cells[25,26]
71 arranged into highly ordered rows and columns[27,28]. Expression of the segment polarity gene
72 *engrailed* is initiated precisely every four rows of the square grid[29]. This emergence and
73 maintenance of square cells across the tissue is particularly striking given that higher surface
74 energy is predicted to be required for this space-packing geometry, and that 4-way vertices, which
75 are essential for square-packing, are unstable in vertex models of epithelia[30]. The amphipod
76 crustacean *Parhyale hawaiensis* is a powerful model for deepening our understanding of how local
77 lineage relationships and physical parameters of individual cells can result in correct tissue
78 morphogenesis and body patterning[31]. In contrast with *D. melanogaster*, in which early patterning
79 is set in motion within a syncytial embryo[32], the early *P. hawaiensis* embryo cleaves
80 holoblastically in a highly stereotyped manner that defines the cellular progenitors of all three
81 germ layers and the germ line as individual blastomeres of the 8-cell embryo[27]. From this stage
82 onwards, the three blastomeres that will give rise to the ectoderm–the descendants of which make
83 up the square-packing epithelium–can be tracked and their clones spatially mapped[27,33].

84 Here we uncover the cellular mechanisms underlying morphogenesis of this highly ordered
85 tissue in *P. hawaiensis*. Previous work in this amphipod suggests that after square cells appear,
86 their packing into a grid is maintained by cell divisions that occur in palindromic medial-to-lateral

87 mitotic waves during the phase when grid rows duplicate along the anterior-posterior axis to
88 establish clonally related parasegments[34]. However, the mechanisms that ensure that 4-way
89 vertices, square cells, and the tissue-wide arrangement of cells into rows and columns emerge in
90 the first place, remain unknown.

91 To address this problem, we used long-term, multiview lightsheet and confocal
92 microscopy, and imaged *P. hawaiensis* embryos from the 16-cell stage through to the first
93 emergence of square cells and the square grid (Fig. 1a). We used semi-automated cell tracking to
94 trace the ectodermal lineages and map their clonal domains onto the quantitative dynamics of cell
95 shape within the expanding epithelium. We show that square-packing geometry emerges along
96 two axes, corresponding with the anterior-posterior and dorsal-ventral body axes, through both
97 lineage-dependent and lineage-independent morphogenetic mechanisms within the tissue. We
98 further show that supracellular actomyosin cables form at these axes, and that the cables are under
99 locally-generated tension higher than that of the surrounding tissue. Finally, we provide evidence
100 that these cables function as a mechanical organizer of this tissue.

101

102 **Results**

103

104 *Ectodermal grid formation*

105 The first seven cleavages of the early *P. hawaiensis* embryo are holoblastic, and the progenitors
106 of all three germ layers and the germ line are established at the 8-cell stage[27,29,33,35]. Beginning at
107 approximately 20 hours post fertilization ("hpf" hereafter), cells that will contribute to the embryo
108 migrate towards the anterior pole and coalesce into an embryonic rudiment referred to as a "germ
109 disk," positioned atop yolk and extraembryonic tissue (Fig. 1d). By 38 hpf, after gastrulation (Fig.

110 1c-e, blue dotted line[33,36]), the ventral surface of this disc (Fig. 1f, h) consists of a monolayer of
111 ectodermal cells[15]. By 68 hpf, the cells in the germ disk have begun aligning into rows and columns
112 and transforming their apical faces into squares (Fig. 1i, j). This square grid sets up the logic of
113 segmentation of the adult body plan (Fig. 1g), with the conserved segment polarity gene *engrailed*
114 becoming expressed along its rows (Fig. 1i-k)[29,37].

115 To visualize this epithelial morphogenesis and its relationship to the ectodermal lineages
116 established at the 16-cell stage (Fig. 1b outside of blue dotted line, Supplementary Fig. 1a), we
117 generated volumetric, long-term timelapse images of *P. hawaiensis* embryos injected with *H2B-*
118 *mCherry* and *Lyn-EGFP* mRNA reporter constructs using multiview lightsheet microscopy (Fig.
119 1a, Movies 1-2). We used a combination of manual and semi-automated methods to annotate cell
120 lineage, cell positions and mitotic activity throughout the entire embryo in frames captured every
121 ten minutes over more than 60 hours of development. We captured the period starting from the
122 eight cell stage at 9 hpf (Stage 4 as per Browne and colleagues[29]) through to Stage 11[29] at
123 approximately 70-74 hpf (Fig. 1a). By the end of the capture period, the ectodermal grid of square
124 cells that is the subject of this study is clearly established (Fig. 1i, i'). We performed this annotation
125 for three embryos, all of which hatched successfully following imaging (Supplementary Table 1).

126 We wished to determine whether and how cell lineage, revealed by the tracking described
127 above, was related to the cell shape dynamics and rearrangements that establish the square grid
128 (Movie 3). However, in the later time-points of these datasets, when the germ disk has expanded
129 over the gradual curve of the embryo's surface, maximum intensity projections of the image
130 volume obscure apical cell morphologies and challenge accurate quantification of cell shape
131 dynamics. To solve this problem, we conformally mapped the 3D surface of the embryo onto a 2D
132 plane using the tissue cartography tool ImSAnE (Fig. 1c')[34,38]. To visualize the grid at even later

133 stages when the square-cell packing geometry has extended throughout the expanding ectoderm,
134 we dissected fixed embryos from the underlying yolk and physically flattened the ectoderm into
135 the 2D plane (Fig. 1h-k). The surface curvature of the unperturbed tissue at these stages is gradual
136 enough that, unlike in some large vertebrate embryos[39], flattening does not require incisions and
137 does not deform cell shapes. Using images of these flattened epithelia, we quantified the dynamics
138 of cell shape change in the ectoderm, as well as the relationship of these dynamics to the lineage
139 relationships of the constituent ectodermal cells, from the 16-cell stage through to the
140 establishment of the grid of square cells that serves as the template for the segmented body plan.
141

142 *Square-packing geometry initiates at a lineage compartment boundary*

143 Previous work has suggested that an ectodermal lineage compartment boundary runs perpendicular
144 to the anterior-posterior axis of the *P. hawaiensis* embryo[40]. Given the early stereotypic cleavage
145 patterns of this embryo, we asked whether lineage could contribute to the initiation of square-grid
146 morphogenesis. We tracked all six of the 16-cell ectodermal lineages (Era, Ela, Erp, Elp, Epr, Epl;
147 Supplementary Fig. 1a; nomenclature as per Gerberding and colleagues[27]) in the lightsheet
148 animations, enabling us to delineate the dynamic lineage territories within the developing germ
149 disk. We observed that a strict boundary emerged immediately after gastrulation between the
150 anterior (Fig. 2a', grey) and posterior (Fig. 2a', striped) lineages, and that clones from each domain
151 never crossed this boundary (Supplementary Fig. 1b, c). This boundary, which we call the
152 initiation line (IL, arrowheads in Fig. 2a), straightened into a line perpendicular to the anterior-
153 posterior axis by 68 hpf (Fig. 2b). The IL was made up of over 30% 4-way vertices from 38-56±2
154 hpf, and of over 40% 4-way vertices by 62±2 hpf (Fig. 2c). This shows that the first emergence of

155 large numbers of 4-way vertices, required for square cell formation, is coincident with the
156 formation of the IL, which is an ectodermal compartment boundary.
157
158 *4-way cellular vertices first emerge in the local vicinity of the IL*
159 Given that 4-way vertices are essential for square cell-packing, and that such vertices first
160 appear in large numbers at the IL, we next characterized the emergence of square cells at the IL.
161 From 38-68 hpf, the cells near the IL exhibited extensive changes in shape and arrangement (Fig.
162 2a). The occurrence of cell rearrangement at the IL was evident by the dynamics of the four 16-
163 cell stage posterior ectodermal lineage domains (Erp, Elp, Epl, Epr; Supplemental Fig. 1a).
164 Whereas in the 26±2 hpf germ disc the Elp and Erp domains were on opposite sides (left and right)
165 of the germ disk, separated from each other primarily by descendants of the anterior Era and Ela
166 clones (Supplementary Fig. 1b, c, top row), they ultimately became separated by a single column
167 of posterior cells descended from one or both of Epl and Epr (Supplementary Fig. 1b, c, bottom
168 row). We also observed cell proliferation throughout the germ disk, including directly at the IL
169 and in the anterior and posterior compartments, throughout this time window (Supplementary Fig.
170 2, Supplementary Table 2).
171 To quantitatively describe the cell shape dynamics, including the transient changes in edge
172 numbers that result from a neighboring cell division and the instability of 4-way vertices[30], we
173 developed a cell shape descriptor metric, defined as the ratio of the area of a cell to the area of the
174 bounding circle of that cell. For this metric, values range from 0.5 to 1, where higher values are
175 closer to hexagons (Fig. 1l). We defined "square cells" as those with values in the range of 0.6-
176 0.66 (darkest color in Fig. 1l). We analyzed the changes in shape in cells along the IL (Fig. 2d, A1
177 and P1), and in cells one cell diameter away from the IL in both the anterior and posterior

178 compartments (Fig. 2d, A2 and P2). At 38 hpf, the rows immediately anterior (A1) and posterior
179 (P1) to the IL had more square cells (> 25%) than other measured regions (Fig. 2d). After 38 hpf,
180 P1 and the row one cell diameter anterior to the IL (A2) had the highest proportion of square cells
181 (20-25%) until 62 hpf, but by 68 hpf the proportion of square cells in A2 dropped to less than 20%
182 (Fig. 2d). The proportion of square cells immediately anterior to the IL (A1), and one cell diameter
183 away posterior to the IL (P2), was similar in both regions from 44 to 68 hpf (Fig. 2d). The
184 proportion of square cells in both regions increased by 68 hpf, comprising the highest proportion
185 of square cells of all measured regions. This gradual and local increase in square cells near the IL,
186 suggests that this lineage boundary initiates and maintains the transition to square-packing
187 geometry along the dorsal-ventral axis.
188
189 *A simulation of cell sorting can explain the emergence of the IL as a straight boundary*
190 Given that the IL is a lineage compartment boundary, we asked whether and how lineage might
191 contribute to the emergence of this first grid axis, which becomes increasingly straight from 26-
192 68 hpf (Fig. 2a, Supplementary Fig. 1b, c). To test the hypothesis that differential behaviors
193 between cells of distinct ectodermal lineages might be responsible for boundary formation, we
194 used CompuCell3D[41–43] to simulate cell sorting within the *P. hawaiensis* ectoderm. To obtain
195 biologically realistic parameters for this simulation, we first segmented lightsheet images at 26
196 hpf, the first time point after the completion of gastrulation, when the surface epithelium is made
197 up entirely of ectoderm cells (Figs. 2a, 3d, Supplementary Fig. 1b). We then quantified the number
198 of cell divisions within each of the six 16-cell stage ectodermal lineages (Fig. 3a) up to 20 hours
199 after this time point (46 hpf). The membrane segmentation and lineage proliferation rates, as well
200 as increased contact energy between the anterior and posterior lineages (Fig. 3b'), were the initial

201 conditions for the simulation. When run, the model consistently (n = 10 runs) produced a straight
202 anterior-posterior compartment boundary as well as a clonal domain mapping like those observed
203 in the actual tissue (Fig. 3e; compare with Supplementary Fig. 1b, c, bottom row). As observed in
204 living embryos (Supplementary Fig. 1b, c), descendants of anterior (Era, Ela) and posterior (Erp,
205 Elp, Epr and Epl) ectodermal founder cells in our model became increasingly mixed with each
206 other anterior and posterior to the IL respectively (Fig. 3c, groups I and II). In contrast, cells on
207 either side of the IL became increasingly segregated over the analyzed time course (Fig. 3c, group
208 III). The results of the model are consistent with the hypothesis that, as observed for ectodermal
209 compartment boundaries in other animal systems[44], the IL is a compartment boundary that is
210 regulated through differential cell sorting among clones.
211
212 *A midline of square cells forms the secondary axis of the grid through intercalation*
213 Previous clonal analyses across multiple species of malacostracan crustaceans have shown that a
214 morphologically distinct column of cells forms along the ventral midline of the embryo[26,27,45–49].
215 The cells of the midline were previously reported to be entirely comprised of Ep descendants
216 (Supplementary Fig. 1a) in *P. hawaiensis*[27], but are described as a polyclone descended from
217 multiple 8-cell stage ectodermal precursors in the related amphipods *Orchestia cavimana*[47,50] and
218 *Gammarus pulex*[46]. We asked whether the *P. hawaiensis* midline played a role in square-cell
219 packing along the anterior-posterior axis of the ectodermal grid, and whether its formation was
220 lineage-dependent. We observed that *P. hawaiensis* midline formation began at 50-60 hpf through
221 sequential mediolateral intercalation[51] of a founder cell population (Fig. 4a-b) in a region we call
222 the intercalation zone (IZ, Movie 4, Fig. 4a'-a''', Supplementary Fig. 3c, d). This region
223 subsequently split into anterior and posterior intercalation zones (Fig. 4a''-a'''), defined as regions

224 of intercalation anterior (IZA) and posterior (IZP) to the IL respectively, as cells aligned at the
225 midline. The IZ founder cell population was identified in the lightsheet datasets by tracking the
226 lineages of aligned cells at 68-70 hpf backwards to the point when only one midline cell was
227 aligned. For the next 10 to 12 hours, the midline elongated (Fig. 4b', c', Supplementary Fig. 3e, f)
228 by a combination of mitotic divisions within the founder population (Fig. 4b', 9-cell midline) and
229 cell intercalation. Midline intercalation started at the IL (arrowheads in Fig. 4a'-a''',
230 Supplementary Fig. 3c-f) and progressed both anteriorly and posteriorly, with the accumulation of
231 midline cells in the anterior zone lagging behind that in the posterior (Fig. 4c). Cells were added
232 to the midline sequentially (Fig. 4c', Movie 4) and each new cell added took its final shape as a
233 square only once it was entirely within the midline (Fig. 4b'). Once aligned, midline cells remained
234 square and were the first square cells formed along the anterior-posterior axis of the grid (Fig. 4a'-
235 a''', Supplementary Fig. 3e, f). To the left and right of this axis, the remaining ectodermal cells
236 first aligned and subsequently transitioned to square-packing in a medio-lateral wave initiated from
237 the midline (Fig. 4a''-a'''). After the 10-12 hour period of midline elongation by intercalation and
238 founder cell division, by 60-72 hpf the midline contained a mean of 8.75 cells in total (Fig. 3c).
239 Subsequently, divisions of parasegment precursor rows[29] in the posterior compartment introduced
240 another mechanism of further midline elongation (starred cells in Fig. 4a''-a''').

241 In contrast with the initiation line, the midline grid axis did not strictly correspond to clonal
242 boundaries between 16-cell ectodermal lineage domains (Supplementary Fig. 3). The emergence
243 of the midline, with the same cell behaviors extending it in both directions along the anterior-
244 posterior axis, spanned the anterior and posterior lineage domains (Fig. 4b, Supplementary Fig.
245 3c, d). However, we observed that the posterior midline was not exclusively made up of Ep
246 descendants (Supplementary Fig. 3c). This is in disagreement with the original lineage tracing

247 report for *P. hawaiensis*[27], but is consistent with the report that embryos lacking an Ep blastomere
248 still form a midline[40]. In the anterior portion of the midline, clones from both anterior ectodermal
249 lineages (Era and Ela) contributed to the midline founder population with no apparent relationship
250 between lineage domains and the anterior IZ (Supplementary Fig. 3a, b). Taken together, these
251 results suggest that the midline initiates the emergence of complete square cells and square-cell
252 packing along the anterior-posterior axis through a highly coordinated morphogenetic process
253 based on cell recruitment rather than inherited fates, as it is not dependent on the 16-cell stage
254 ectoderm lineages (Supplementary Fig. 3).
255
256 *The initiation line and midline axes are tensile cytoskeletal cables*
257 Given the emergence of square-cell packing geometry first at the IL (around 30 hpf) and
258 subsequently at the midline (around 50 hpf), we hypothesized that these boundaries introduce
259 tension into the tissue to initiate the transition to square-packing. To test this hypothesis, in *P.*
260 *hawaiensis* embryos stained with phalloidin (Fig. 5a) and injected with a myosin 2 mRNA reporter
261 construct (based on the *P. hawaiensis* ortholog of the *D. melanogaster spaghetti-squash* gene
262 [52] (*Ph-sqh*), Supplementary Fig. 4), we measured the relative amounts of filamentous actin (f-
263 actin) and myosin 2 at the IL when it appeared in earlier stages (38-56 hpf, Fig. 5a-a'), and on
264 either side of the midline when it formed at later stages (around 68-74 hpf, Fig. 5b, b').
265 In 38-56 hpf embryos, we found significantly higher levels of f-actin (Fig. 5a, a') and
266 myosin 2 (Supplementary Fig. 4a, a') at the IL relative to the equivalent region of interest (ROI)
267 one cell anterior (IL/A1) or posterior (IL/P1), compared with one to two cells posterior (P1/P2).
268 Similarly, we also found significantly higher levels of f-actin on the left (ML) and right (MR) sides
269 of the midline in embryos with 6-15 cells in the midline (68-74 hpf) (Fig. 5b, b') compared with

270 the equivalent ROIs one and two cells to the left (ML1, ML2) and right (MR1, MR2). In contrast,
271 levels of myosin 2 on either side of the midline were not significantly higher than the ROIs to the
272 left and right of the midline (Supplementary Fig. 4b'b"). We hypothesize that these accumulations
273 of cytoskeletal proteins constitute supracellular cables running along the two axes of the
274 ectodermal grid (Supplementary Fig. 5).

275 In *D. melanogaster*, actomyosin cables segment embryonic and larval tissues by
276 introducing local tension into the tissue[19,53,54]. We hypothesized that the supracellular cables we
277 detected in the *P. hawaiensis* germ band were similarly under tension, allowing them to regulate
278 the formation of the first square cells in the grid. To test this hypothesis, we cut the cables with a
279 pulsed laser tuned to 927 μm and measured subsequent tissue recoil around the incision site (Fig.
280 5c, dashed line and arrows). In 38-44 hpf embryos that had formed the IL, recoil lengths were
281 significantly (1.5 to 2.5-fold) higher at the IL compared with control cuts made four to seven cells
282 anterior to the IL (Fig. 4c'). Interestingly, this increase is comparable to the mean of 2.37-fold
283 higher tension reported at the *D. melanogaster* wing disc anterior-posterior compartment boundary
284 compared with that at cell edges within the anterior or posterior tissue compartments[53]. In embryos
285 live-imaged following the IL cut, we observed that the 4-way vertices surrounding the incision site
286 remained intact (black arrowheads in Fig. 5c), suggesting that maintaining a square shape at the
287 IL is not dependent on tension in neighboring cells.

288 In later stage embryos in which 3-6 cells had aligned into the midline (58-69 hpf), recoil at
289 midline cables in the posterior IZ was significantly (2 to 3-fold) higher than at other non-IZ regions
290 one to four cell diameters anterior or lateral to the midline (Fig. 4c"). In contrast, recoil lengths at
291 the cables in the anterior region of the midline where intercalation had finished and cells were
292 square in shape (P1 in Fig. 5b, c") were not significantly different than those at the lateral and

293 anterior control regions (Fig. 5c”). To determine whether tension was mechanically coupled across
294 cells contributing to the cable, we measured the recoil of a second cut in the midline after making
295 a first cut two to three cells away in the cable (Fig. 4c’), and found that P1 and IZ second cut
296 recoils were not significantly different from those at first cuts (Fig. 5c”). We note that a similar
297 phenomenon of local, potentially cell-autonomous contribution to tension across a supracellular
298 actomyosin cable spanning many cell diameters, has also been reported in the morphogenesis of
299 an extra-embryonic membrane in the beetle *Tribolium castaneum*[55]. Taken together, these results
300 suggest that there are supracellular cables under tension at the IL and at the midline, and that
301 tension within midline cables is heterogeneous and locally generated.

302 Tension in actomyosin cytoskeletal cables results from the phosphorylation of the
303 regulatory light chain of myosin 2, which slides the attached actin filaments past one another[56].
304 The results of our laser ablation experiments suggested that while both the IL and the midline
305 cables possessed supracellular actomyosin cables that were under tension, tension at IL was not
306 essential for the formation of 4-way vertices. This led us to hypothesize that abrogation of myosin
307 2 phosphorylation would not hinder square cell-packing geometry formation at the IL at earlier
308 stages, but might disrupt square cell formation at the midline at later stages.

309 To test this prediction, we first assessed the effect of sustained elimination of myosin 2
310 phosphorylation during the later stages. We focused on the period when intercalation is the only
311 mechanism of midline formation (50-68 hpf, Fig. 4b, b’), and chose morphologically stage-
312 matched embryos in which just one cell had aligned into the midline (50-56 hpf, Fig. 4b) for
313 incubation in 50μM of the Rho-kinase inhibitor Rockout for 12 hours (Fig. 5d, d’). This
314 concentration of Rockout did not impact normal cell proliferation (Supplementary Fig. 6a, b),
315 thereby allowing the thresholds of contractility needed for cytokinesis[19,54]. Rockout-treated

316 embryos at this stage had significantly fewer cells aligned into the midline than controls (mean 1.4
317 vs 6.4, Fig. 5f) but maintained the same total number of cells in the posterior compartment (Fig.
318 5f'). Notably, a relatively straight boundary at the IL was maintained in the midline Rockout-
319 treated embryos (Fig. 5d', arrowheads). In contrast, earlier stage embryos (38 hpf) treated for 12
320 hours in 50μM Rockout had, by 50 hpf, percentages of 4-way vertices that were not significantly
321 different from controls (Fig. 5e). Taken together, these results suggest that while 4-way vertices
322 first appear at the IL (Fig. 2), their maintenance is not dependent on the phosphorylation of myosin
323 2 (Fig. 5e). In contrast, however, subsequent establishment of the first square cells is dependent
324 on the contractility of myosin 2 within midline cables (Fig. 5g).
325
326 *The midline cables organize square-cell packing and the emergence of a stripe of Engrailed-*
327 *positive cells*
328 Given the presence of differential tension within the germ disk (Fig. 5c, c"), and the midline as the
329 initiation site of the transition to square-packing along the axis of grid elongation (Fig, 4,
330 Supplementary Fig. 3), we hypothesized that localized mechanical perturbation of the midline
331 would disrupt the organization of square-cell packing across the tissue, and that perturbing square-
332 cell packing would in turn have consequences for the correct establishment of segments. To test
333 this, we performed two classes of physical ablations, either directly at the midline (Mid), or three
334 cell diameters lateral to the midline (Lat) in embryos in which 3-6 midline cells had aligned (58-
335 69 hpf, A: pink rectangles in Fig. 6b, c). The contralateral side of the same embryo, which was not
336 ablated (NA: pink rectangles in Fig. 6b, c), served as an internal control. In the resulting four
337 experimental groups (Mid-A, Mid-NA, Lat-A, Lat-NA), we analyzed posterior compartment cell
338 shapes (Fig. 6d, d'), number of cells in the midline (Supplementary Fig. 7), and expression of the

339 segment marker Engrailed[37] (En, Fig. 6e, Supplementary Table 3) 9-12 hours after ablation. In the
340 100 closest cells to P1 posterior to the IL, we used Kernel density estimation[57,58] to estimate the
341 cell shape probability densities for all groups, including wild type embryos morphologically stage-
342 matched to Lat embryos based on the number of cells in the midline. We plotted the deviation of
343 the four experimental groups from the wild type distribution over the range of cell shape values
344 observed (Fig. 6d').

345 We found that at 38 hpf, ablations of the IL and control ablations three cell diameters
346 anterior to the IL did not prevent the formation of square cells nor the establishment of the
347 ectodermal square grid (Supplementary Fig. 8). Additionally, 38 hpf embryos in which we made
348 a single cut in the IL cable maintained a straight line at the IL region of the tissue and began
349 midline formation 12 hours later (Supplementary Fig. 8). This is consistent with the observation
350 that 4-way vertices still form correctly after inhibition of myosin 2 phosphorylation at IL
351 establishment stages (Fig. 5e).

352 In contrast, in embryos in which 3-6 midline cells had aligned (58-69 hpf), ablations lateral
353 to the midline significantly perturbed the cell shape distribution on the ablated side of the embryo
354 (Lat-A, Fig. 6d) compared with the unablated side (Lat-NA), overall driving them towards a
355 rounder, rather than square, shape (Fig. 6b', d'). Relative to wild type, Lat-NA exhibited the
356 smallest increase in anisotropic cells (defined as those with a cell shape metric value of $\leqslant 0.5$;
357 circle (i) in Fig. 6d') and the smallest decrease in square cells (circle (ii) in Fig. 6d') of all four
358 groups.

359 Unlike the localized impact of lateral ablations, midline ablations significantly disrupted
360 cell shape distributions both on the ablated side (Mid-A) and on the contralateral control side (Mid-
361 NA) (Fig. 6c',d'). On both sides of midline ablated embryos, more cells took on more irregular

362 shapes, characterized by lower values of the cell shape metric (Fig. 6d). In particular, the
363 proportion of square cells was significantly lower than wild type in both the experimental and the
364 control (contralateral) group of midline ablations (circle (ii) in Fig. 6d'). Midline ablation
365 destroyed the organization of the square-packed grid throughout the posterior germ rudiment (Fig.
366 6c'). In sum, the effect of the lateral ablation was minimal and localized to the region immediately
367 around the ablation, while perturbing just one of the midline cables had a tissue-wide impact on
368 cell shapes, disrupting square cell formation and abolishing the square ectodermal grid.

369 Midline, but not lateral, ablations also disrupted midline elongation. Laterally-ablated
370 embryos developed midlines with total numbers of cells comparable to wild type (12-19 cells,
371 Supplementary Fig. 7) while midlines in midline-ablated embryos were shorter (5-10 cells,
372 Supplementary Fig. 7). This suggests that midline cable ablations, but not ablations lateral to the
373 midline, disrupted posterior intercalation at the midline. These data are consistent with the
374 hypothesis that the alignment of cells into the midline, driven by the contractility of the midline
375 cables, organizes cell shape across the tissue.

376 Finally, we asked whether establishment or maintenance of the square cell grid was
377 important for correct segment patterning. At stage 11-12 of embryogenesis (66-68 hpf[29]), when
378 midline elongation by intercalation has completed (Fig. 4a"), the protein product of the
379 segmentation gene *engrailed* (En) becomes detectable in two cells anterior to the IL, initially in a
380 few cells within the same row at or near the midline[29]. The En expression domain subsequently
381 expands in an increasing, left-right symmetrical number of lateral cells within the row[29]. This
382 expression marks the prospective mandibular segment (Mn, arrowhead in Fig. 1i, j)[29,45].
383 Subsequent rows of En-expressing ectodermal cells, delineating the remaining segments of the

384 body plan, arise correlated with the same stereotyped cell divisions of the cells in the grid that
385 contribute to midline elongation (Fig. 1j, k) [29,45].

386 Given that En expression in the prospective mandibular segment is detected right after the
387 midline intercalation phase that appears to create the first square cells in the grid, we asked whether
388 this expression was dependent on the tensile midline cables in the same way as square cells and
389 square-packing order. Across the WT and ablated samples, we found that the total number of
390 Engrailed-positive nuclei in the prospective mandibular segment was positively correlated with
391 the number of aligned midline cells (Supplementary Fig. 7b, Supplementary Table 3). In other
392 words, as the midline became longer, more lateral cells within Mn expressed En. Strikingly,
393 however, midline ablation reduced the number of En-positive Mn nuclei, even on the contralateral
394 control side of the embryo (Figure 6e, Supplementary Table 3). In contrast, lateral ablations had
395 little impact on the number of Engrailed-positive Mn nuclei on either the experimental or the
396 control side of the embryo (Figure 6e, Supplementary Table 3). Midline but not lateral ablations
397 also decreased the regularity with which Mn cells expressed En (Figure 6e, Supplementary Table
398 3). Given these results, we hypothesize that the first establishment of En expression across a
399 complete segment, as seen in Mn, requires midline-cable driven tissue organization.
400

401 **Discussion**

402

403 *The role of cell lineage in initiating square cell formation*

404 We found that descendants of the 16-cell stage ectodermal founder blastomeres segregate into
405 anterior and posterior compartments, and that the resulting compartment boundary (IL) forms the
406 first axis of the square cell grid. This suggests the possibility that cell lineage at least partly

407 underlies square cell morphogenesis. The results of our simulation suggest that cell sorting
408 between the cells of the anterior and posterior compartments, a phenomenon observed in multiple
409 contexts in animal development including amphibian embryos[59] and *Drosophila* imaginal discs[60],
410 regulates the formation of a straight compartment boundary. The mechanism that regulates this
411 cell sorting could in principle be one or more of differential cortical stiffness[61–63], differential
412 adhesion[44,62–67], or a mechanical barrier imposed by the supracellular actiomyosin cable that forms
413 at the IL. Relevant to the latter hypothesis, we note that although the cable at the IL is under
414 tension, coupled tension and the phosphorylation of myosin 2 are not required to maintain 4-way
415 vertices at this boundary. This suggests that local tension at this IL cable is not necessary to
416 maintain the compartment boundary. Alternatively, it is possible that the interaction between the
417 anterior and posterior lineages can regenerate the tensile cable upon ablation.

418 The results of previous experiments demonstrating that the *P. hawaiensis* early embryonic
419 ectoderm has regulative capacity are interpretable as consistent with the cell sorting hypothesis[40].
420 In these experiments, individual 8-cell stage ectodermal blastomeres were photoablated and the
421 remaining two blastomeres were injected with a lineage tracer. The results showed that El and Er
422 can replace each other's anterior descendants, while Ep can replace their posterior descendants[40].
423 We hypothesize that compensation within the ectoderm, and ultimately grid formation, is possible
424 only when progenitors of both anterior and posterior lineages remain, and that cells from both
425 compartments are necessary to initiate square cell-packing geometry at the IL. Under this
426 hypothesis, both anterior and posterior cell types would be needed to form the boundary because
427 each lineage would contribute a distinct molecular state (e.g. cortical stiffness and/or adhesive
428 properties), the combination of which would then lead to emergent cell sorting.

429 In embryos of diverse animal species–including *D. melanogaster*[68–70], the flour beetle
430 *Tribolium casteneum*[55], the cnidarian *Hydra vulgaris*[71], the zebrafish *Danio rerio*[72], and the quail
431 *Coturnix japonica*[73]–mechanically integrated actomyosin cables spanning multiple cells play
432 crucial roles in epithelial morphogenesis. We hypothesize that differential genetically-determined
433 fate between the anterior and posterior lineages also underlies the assembly, and potentially the
434 shape organizing function, of the cytoskeletal cable we observed at the anterior-posterior boundary
435 (IL) from 38 hpf onwards, similar to anterior-posterior boundary formation in the *D. melanogaster*
436 wing disc[53]. In the early *Caenorhabditis elegans* embryo, both endodermal cell fate and the
437 phosphorylation of myosin 2, which are necessary for gastrulation in endodermal cells, are
438 dependent on the Wnt-Frizzled signaling pathway, suggesting a direct connection between cell
439 fate and morphogenesis[74]. A similar relationship could exist within the *P. hawaiensis* ectoderm,
440 the molecular determinants of which have yet to be identified.
441 Further ablation experiments in 16-cell stage embryos that eliminate all anterior or
442 posterior lineages, or elucidation of the transcriptomic, proteomic and mechanical states of the
443 anterior and posterior compartment clones, would be useful to elucidate the mechanism of cell
444 sorting at the IL. A hypothesis of one or both of differential adhesion or differential cortical
445 stiffness would predict that anterior and posterior cells have different levels of cell-cell adhesion
446 molecules and/or different cortical cytoskeletal behaviors. The fact that the IL marks a clonal
447 boundary could in principle provide a heritable mechanism of achieving differential molecular
448 states between clones. For example, anterior cells might inherit a level of adhesion molecules or a
449 cortical cytoskeletal conformation distinct from that of their posterior neighbors by virtue of
450 differential inheritance of cytoplasmic factors, or through inheritance of a gene regulatory state.
451

452 *The role of mechanical stimuli in establishing square cell packing*

453 Once the IL has straightened into an actiomyosin rich boundary axis, we found that a
454 midline cell founder population begins to intercalate perpendicular to the IL such that square cells
455 are added sequentially to the midline between two actiomyosin cables. This grid axis does not
456 correlate with 16-cell lineage domain boundaries, such that the midline founder population is a
457 polyclone containing descendants of multiple ectodermal founders (Supplementary Fig. 1, 2).
458 These findings suggest that, unlike the IL, the formation of the midline and its cables is not
459 regulated by inherited differences among these lineages. We hypothesize that the midline grid axis
460 is instead initiated by mechanical stimuli, similar to how the formation of the primitive streak in
461 early avian embryos, which involves anterior-posterior oriented actomyosin cables[75], is driven by
462 tissue flows that regulate the expression of fate-determining genes.[9] Under this hypothesis, the
463 midline founder population would become defined–and, in turn, potentially genetically
464 differentiated–as a result of tissue-wide forces. Future work could examine whether fate-
465 determining genes of this population include components of the planar cell polarity signaling
466 pathway, which is involved in medio-lateral intercalation of mouse kidney tubules.[76]

467 We have provided evidence that the mechanical integrity of these midline cables is
468 necessary for the formation of isometric cells, the alignment of cells into rows, the maintenance
469 and packing of square cells across the ectodermal grid, and the establishment of segmentally
470 iterated En expression. We hypothesize that these cables drive tissue-wide mechanics, just as tissue
471 flows pattern the retina[77] and embryonic germ band extension[78] in *D. melanogaster*, or how
472 supracellular actin cables organize whole body regeneration in *H. vulgaris*[71]. In this framework,
473 the tension introduced by the midline cables at the intercalation zones could be the initial condition
474 necessary to trigger and perhaps subsequently balance the transition to square-packing. The

475 variance in recoil times in response to ablation at the IL and midline intercalation zones (Fig. 5c',
476 c"), suggests that tension at these regions could be dynamically modulated in response to global
477 tissue forces.
478
479 *The relationship between square-cell packing, gene expression, and segmental patterning*
480 In ascidian and mouse embryos, cell geometry is crucial for the expression of fate-determining
481 genes[79,80]. Our study suggests that in *P. hawaiensis*, square grid morphogenesis and subsequent
482 segment formation emerge from axes that are established according to differing degrees of
483 instruction from tissue mechanics and genes. We also provide evidence that expression of the
484 segment polarity gene *en* in the *P. hawaiensis* ectoderm is sensitive to mechanical perturbation
485 and dependent on the formation of the midline. Reminiscent of this finding, in *D. melanogaster*
486 embryos injected with paramagnetic-beads and subjected to ectopic tissue-wide forces with
487 magnetic tweezers, expression of En at parasegment boundaries was differentially altered
488 according to the location and magnitude of the force[81]. The authors of that study observed a change
489 in nuclear shape and redistribution of myosin 2 in tissue regions experiencing the applied force,
490 suggesting that expression of *en* is downstream of these mechanical and geometric parameters[81].
491 This raises the possibility that mechanical regulation of *en* expression could be a conserved feature
492 in multiple pancrustacean species.
493 In early *D. melanogaster* embryos, membrane fluidization by an ether treatment applied to
494 whole embryos results in larvae with a dramatic range of segmentation defects, from complete loss
495 of segments to the elimination of only a single segment, which resembles segmentation gene loss
496 of function phenotypes[82]. Our *P. hawaiensis* midline ablation experiments, in which cuts were
497 made in the exact same cell positions across samples, similarly resulted in a range of changes in

498 cell shape, midline cell number, and *en* expression, suggesting that segmentation in *P. hawaiensis*
499 could arise from a balance of tuned forces within the ectodermal epithelium. In this mechanical
500 framework, the ultimate effect of midline cable disruption could depend on the mechanical state
501 elsewhere in the tissue. Further experiments determining the longer-term effect of early midline
502 disruption, and the alteration of square-cell packing, on the formation of more posterior segments
503 will be necessary to establish the extent of the midline cables' organizing capabilities.

504 Beyond amphipods, previous comparative studies of embryogenesis in other malacostracan
505 orders (including Cumacea, Tanaidacea, Isopoda, and Mysidacea) have found that they generate
506 some of the cell material for their ectodermal grids through consecutive divisions of ectodermal
507 stem cells (ectoteloblasts) that provisionally align their clonal progeny into rows in the posterior
508 portion of the grid[83]. However, ectodermal grids in these species also contain cells derived from
509 non-ectoteloblast lineages, suggesting that some other mechanism of tissue organization must be
510 present[28]. Amphipod grids like that of *P. hawaiensis* completely lack ectoteloblasts and thus must
511 be organized by what Wolfgang Dohle and Gerhard Scholtz called a "row-forming factor," which
512 they hypothesized to be a "matrix forcing the cells into a grid-like pattern"[83]. Our results suggest
513 that this "matrix" emerges first from tensile cell-sorting at the IL and subsequently from
514 cytoskeletal cables at the midline. *O. cavimana*, another amphipod, exhibits stereotypic early
515 cleavage patterns similar to that of *P. hawaiensis*, suggesting that fate determination within the 8-
516 16 cell embryo could also play a role in grid morphogenesis of this species[47]. Further lineage
517 studies across the Amphipoda, the early embryos of which all undergo holoblastic cleavage[84], are
518 needed to understand the full extent of this mechanism within this group.

519 The amphipod anterior-posterior compartment boundary corresponds to a boundary
520 classically called the naupliar-post-naupliar boundary. Under this concept, the naupliar region of

521 the germ band, is the anterior region that will give rise to the head and mandibular segments,
522 formed through a combination of relatively uncoordinated mitoses, cell intercalation, and cell
523 rearrangements, and the post-naupliar region. In contrast, the post-naupliar germ band is formed
524 through the activity of either ectoteloblasts or segment precursor row duplications[45,46,85], and gives
525 rise to the trunk segments and telson. Interestingly, our work shows that the IL, positioned one cell
526 diameter posterior to the first complete segmental stripe of En expressio in the prospective
527 mandibular segment, corresponds to the classically defined naupliar-post-naupliar boundary.

528 The anterior-posterior compartment boundary is established by the descendants of
529 ectodermal lineage precursors defined by stereotypical holoblastic cleavages[27,33] and likely also
530 by asymmetric inheritance of lineage potential to early blastomeres that begins at first
531 cleavage[35,86,87]. However, holoblastic cleavage is a derived state for the Malacostraca, in which
532 many extant species undergo syncytial cleavage[47], and the ancestral cleavage state is thought to be
533 meroblastic (in which cleavage furrows form but cytokinesis is not completed, effectively resulting
534 in a syncytium but with some partial yolk partitioning by the formation of incomplete furrows)[88,89].
535 We speculate that the evolution of holoblastic cleavage in amphipods facilitated the emergence of
536 lineage-based IL formation and the anterior-posterior compartment boundary as a mechanism for
537 establishing the ectodermal grid and generating the post-naupliar germ band. Under this
538 hypothesis, the evolution of an anterior-posterior boundary among the ectoderm clones eliminated
539 the need for patterning introduced by a row of proliferating ectoteloblasts within the germ disk.
540 With regards to grid organization along the anterior-posterior axis, we hypothesize that midline
541 formation via intercalation, and the importance of the mechanical organizing properties of the
542 midline for establishing correct segmental patterning, are likely to be conserved across the

543 Malacostraca. Further comparative studies should determine whether midline cables are present in
544 other species.
545
546 **Methods**
547
548 *Animal culture and transgenesis*
549 *P. hawaiensis* were cultured at 26 ºC in 16-quart plastic tanks containing 1.022 specific gravity
550 Instant Ocean artificial sea water (hereafter ASW) made with distilled water and fed a diet of
551 TetraPro PlecoWafers and fresh carrots. For live imaging of nuclei (Fig. 4c) we used a previously
552 reported[90] transgenic *P. hawaiensis* line in which the *D. melanogaster* histone H2B fused with a
553 monomeric Red Fluorescent Protein is under control of a *P. hawaiensis* heat-shock promoter
554 (hereafter *H2B-mRFPruby*).
555
556 *Embryo collection and microinjection*
557 Embryos for all experiments were collected and microinjected according to established
558 protocols[91]. Embryos were collected into and cultured in ASW filtered with a 0.22µm filter
559 (hereafter FASW). For precise staging and stage-matching among broods, only 1-cell through 8-
560 cell stage embryos were collected. All microinjected embryos were injected at the late 1-cell stage
561 once the chorion had hardened. Microinjected embryo cultures were supplemented with 1:100
562 Penicillin-Streptomycin (10,000 U/mL penicillin, 10,000 µg/ml streptomycin; Gibco 15140-122)
563 and 1:200 Amphotericin-B (250 µg/ml, Gibco 15290-026). The culture medium was changed out
564 every 1-2 days. For live imaging of actin, embryos were injected with 180pl of 2 µg/µl of an
565 mRNA reporter construct transcribed *in vitro* with a mMessage mMachine T7 kit (Invitrogen

566 AM1344) from a pBSK plasmid in which LifeAct[92] was fused to a monomeric mNeonGreen
567 coding sequence[93] (hereafter *LifeAct-mNeonGreen*). Myosin 2 was visualized by injecting 180pl
568 of 2 µg/µl of an mRNA construct in which the *P. hawaiensis spaghetti-squash* ortholog (*Ph-sqh*)
569 coding sequence was fused to mNeonGreen (hereafter *Ph-sqh-mNG*). For long-term lightsheet
570 imaging of cell membranes and nuclei, embryos were co-injected with mRNA constructs
571 transcribed *in vitro* from PCS2 + H2A-mCherry:pDest (hereafter *H2A-mCherry*) and PCS2 + Lyn-
572 GFP (hereafter *Lyn-GFP*) plasmids. Cloning details of all constructs are available upon request.
573
574 *Immunohistochemistry and drug treatments*
575 Embryos were dissected away from their outer membrane according to established protocols[94] and
576 fixed for one hour at room temperature in 4% paraformaldehyde made up in FASW. Fixed tissue
577 was immediately transferred into a blocking solution (1x phosphate buffered saline (1x PBS) +
578 5% normal goat serum + 0.1% Triton X-100) or stored at 4 ºC in 1x PBS + 0.1% Triton X-100 for
579 up to three days prior to staining. Embryos were stained with 1:100 AlexaFluor 488 Phalloidin
580 (Invitrogen A12379) or Rhodamine Phalloidin (Invitrogen R415) for f-actin, 1:1000 rabbit anti-
581 Myosin 2 656[95], 1:80 mouse anti-Engrailed Mab 4D9[37], 1:500 mouse anti-phospho-histone H3
582 (Cell Signaling 9706S), or 1:50 rabbit anti-cleaved caspase-3 conjugated to AlexaFluor 555 (Cell
583 Signaling 9604S) overnight at 4ºC. We followed these incubations with a solution containing
584 1:10,000 Hoechst 33342 (Sigma B2261, 10 µg/µl stock solution) as well as secondary antibodies
585 1:500 AlexaFluor 647-conjugated Goat Anti-Mouse (Invitrogen A31625) or 1:500 AlexaFluor
586 555-conjugated Goat Anti-Mouse (Invitrogen A31621) in blocking solution for two hours at room
587 temperature. Prior to fixation, drug-treated embryos were cultured for 12 hours at 26ºC in a
588 solution of Rockout (Rho Kinase Inhibitor III, Sigma 55555-3) dissolved in anhydrous DMSO and

589 added to a 30mm petri dish containing 6ml of 50% FASW, as previously described[36]. We found
590 that a 50µM concentration of Rockout did not disrupt normal cell proliferation and that 100% of
591 38 hpf-treated embryos survived up to two days in a continuous treatment (Supplementary Fig. 6).
592 Embryos cultured in 50% FASW alone at 26ºC, or with the equivalent amount of DMSO, hatched
593 normally (Supplementary Fig. 6).
594
595 *Microscopy*
596 Embryos for multiview lightsheet imaging were injected at the 1-cell stage with 2 µg/µl *H2A-*
597 *mCherry* (nuclei) and *Lyn-GFP* (membrane) mRNA reporter constructs. We mounted 4-cell stage
598 embryos inside of a 2mm PTFE tube and 3mm glass capillary suspended in 1% low melt agar
599 made in filtered ASW and infused with fluorescent beads (Estapor Microspheres). Capillaries were
600 mounted on a SiMView multiview lightsheet microscope[96] and embryos imaged with a 488 nm
601 (*Lyn-GFP*) and 555 nm (*H2A-mCherry*) laser at ten-minute intervals from three or four angles
602 with two objectives positioned 180º apart. The z-interval was set to 0.41µm. The resulting six or
603 eight views per sample were registered and fused using the MultiView Reconstruction and
604 BigDataViewer plugins for Fiji[97–100].
605 Live imaging of *H2B-mRFPruby* transgenic embryos and *LifeAct-mNeonGreen* or *Ph-sqh-*
606 *mNG* mRNA injected embryos was carried out at 26ºC on a Nikon CSU-W1 SoRa Spinning Disk
607 confocal microscope with a 20x objective. Embryos were mounted individually on glass
608 microscope slides so that a 1.5 coverslip with clay-feet spacers could be used to roll the desired
609 region of the germ-disc or grid into the field of imaging. We applied slight pressure to the coverslip
610 to flatten the tissue and obtain clearer views of apical cell face geometries. We then filled the space
611 between the coverslip and slide with FASW and sealed the edges with Vaseline to prevent

612 evaporation. Time-lapse imaging of live embryos was carried out at ten-minute intervals with a z-
613 interval of 0.9µm. Fixed and stained embryos were cleared in 70% glycerol and mounted
614 individually in the same manner as live embryos for confocal imaging on either a Nikon CSU-W1
615 SoRa Spinning Disk (0.9µm z-interval) or Zeiss LSM 880 (1µm z-interval). Only timelapse
616 datasets taken of embryos that hatched successfully were used for analysis.
617
618 *Image analysis and segmentation*
619 Lineage tracing of the fused lightsheet datasets was performed with either semi-automated
620 (Embryo 1; Supplementary Table 1) or manual tracking (Embryos 2 and 3). The nuclear channel
621 of Embryo 1 was first pixel classified and then object tracked in ilastik[101] (ver. 1.3.3), followed by
622 manual correction in MaMuT[90] (ver. 1.53), a plugin for Fiji. Embryos 2 and 3 were tracked entirely
623 manually using both the nuclear and membrane channels in MaMuT [90] or Mastodon in Fiji. We
624 created the 2D conformal maps of the embryo's surface from the lightsheet datasets using a version
625 of ImSAnE[102] customized for *P. hawaiensis*[34]. Nuclear tracks colored according to 16-cell stage
626 lineages were superimposed onto the maps using a custom MATLAB script or manually
627 superimposed in Adobe Illustrator (CC 2023 or 2024). Maximum intensity projections of the
628 lightsheet 2D conformal maps of *Lyn-GFP* (membrane marker) were segmented in the Fiji plugin
629 TissueAnalyzer[103] using a watershed algorithm with manual correction.
630 To visualize and quantitatively describe cell shapes, we first pixel-classified membranes in
631 10µm maximum intensity projections of Phalloidin-stained or *LifeAct-mNeonGreen*-labeled
632 embryos in ilastik[101] (ver. 1.4.0) to generate a more consistent cell boundary signal. Especially in
633 the later grid stages (approximately 62 hpf onwards), the embryo must be carefully laid flat against
634 the slide and slightly compressed with the coverslip. For samples in which flattening out all

635 wrinkles or depressions in the tissue was not possible, the probability maps containing apical cell
636 faces for each tissue region were cut out and composited together using the Image Calculator in
637 Fiji. We then fed the probability maps exported from ilastik[101] (ver. 1.3.3) into Cellpose[104] (ver.
638 3.0) and obtained cell ROIs using a custom-trained model with some manual correction of
639 contiguous masks. Automatic size calibration was performed and non-contiguous or incomplete
640 cell masks around the edges were removed. All subsequent quantitative descriptions of cell shape
641 and tissue organization were carried out on these ROIs using custom Python scripts available at
642 https://github.com/boyonpointe/parhyale_morpho/tree/main with commit ID a19a88d. All other
643 measurements, including intensities of cytoskeletal components, were made on 10µm maximum
644 intensity projections in Fiji (ver. 2.1.0) using the ROI section and associated measurement tools.
645 For cell shape and vertex IL measurements, each 10 µm maximum intensity projection
646 was cropped to 207 µm wide x 104 µm high. The crop box was centered on the germ disk
647 parallel to the dorso-ventral axis and centered on the midpoint of the IL (a clear straight or
648 slightly bent line) in the anterior-posterior axis. Only cells contained fully within the crop box
649 were counted.
650 For IL actin and myosin 2 measurements, in un-cropped 10 µm maximum intensity
651 projections, the lateral extent of the IL region of interest was determined by drawing a line from
652 the ventral midline of the germ disk towards the left and right sides of the germ disc. The region
653 was considered terminated when it reached cells whose sides were bent more than approximately
654 15º from the leading edge of the region. The mean IL length for phalloidin-stained samples (f-
655 actin) was 146 µm (n = 38) and the mean IL length for *Ph-sqh*-labeled samples (myosin 2) was
656 151 µm (n = 14).

657 To compare cell shape distributions in the posterior of the germ disc, we used a bootstrap
658 approach. For each pair of distributions, we generated 100,000 surrogate pairs of random
659 resampling and calculated the difference in their means. This gave us a null distribution of
660 differences, against which we assessed how often the observed empirical difference would occur.
661 The p-value corresponds to that probability. For stop motion in Movie 3, images were printed on
662 light-permeable paper and animated over a lightbox using a Sony A7S camera controlled by the
663 stop-motion animation software DragonFrame (v4).
664
665 *Cell shape descriptor*
666 To measure cell shape, we used a custom descriptor in which the area of a cell face is divided by
667 the area of the circle whose diameter is equal to the distance between the farthest two points on
668 the cell's perimeter. With this descriptor, a perfect square has a value of 0.64, and hexagons and
669 higher order polygons have values of approximately $\geqslant 0.75$. We found this measurement to more
670 usefully describe the emergence of square-cell packing than counting the number of cell sides,
671 because within this dynamic tissue, 4-way vertices frequently dissolve into small edges at square
672 corners, and cell divisions can introduce temporary kinks into neighboring cell edges.
673
674 *Ablation experiments*
675 Ablation experiments were carried out on a Zeiss 980 NLO 2-photon microscope with a pulsed
676 Spectra-Physics InSight X3+ laser set to 927 μm wavelength and an ablation ROI with a 1μm
677 width that was passed over five times. *LifeAct-mNeonGreen* embryos injected at the 1-cell stage
678 were incubated to the desired stage and mounted individually on slides with a Vaseline-sealed
679 coverslip. Ablated embryos were imaged with a LD LCI Plan-Apochromat 25x/0.8 objective for

680 two frames prior to the ablation followed by every second for two minutes immediately afterwards.
681 Some embryos were further imaged on the same microscope at intervals of one minute to follow
682 the effects of the ablation. Embryos used for further analysis were then recovered from the slide
683 and transferred to a 35mm petri dish with fresh FASW with 1:100 Penicillin-Streptomycin (10,000
684 U/mL penicillin, 10,000 µg/ml streptomycin; Gibco 15140-122) and 1:200 Amphotericin-B (250
685 µg/ml, Gibco 15290-026) for incubation at 26 ºC until fixation. Recoil length was calculated in
686 Fiji by subtracting the distance between cell vertices on either side of the ablation ROI in the first
687 frame immediately post ablation, from the distance between the same two vertices before the
688 incision was made.
689

690 *Figure presentation*

691 Line tracing of membranes shown in figures was performed using the Image Trace function
692 (Silhouettes or Line Art) on exported Cellpose[104] ROIs or on hand segmented micrographs
693 (Supplementary Fig. 3) in Adobe Illustrator 2024 or 2025. To more clearly display the
694 relationship between Engrailed expression and grid geometry in Figure 1, we used ilastik[101]
695 (ver.1.3.3) to pixel-classify images of anti-Engrailed staining and exported the resulting
696 probability maps. In Movie 4, TissueAnalyzer[105] was used to track and visualize cell membranes
697 of the midline founder population in a conformally mapped time-series that was manually
698 aligned. All figures were assembled with Adobe Illustrator.

Acknowledgements
The authors thank Sebastian Streichan and Dillon Cislo for help with ImSAnE and applying MaMUT tracks to ImSAnE maps, as well as members of the Extavour and Pavlopoulos laboratories for discussion.

Author Contributions
BS conceived of the study, designed experiments, performed all wet lab experiments, performed data analysis and interpretation, and wrote the first draft of the manuscript. LB designed, performed embryo collection and injection experiments for, and executed capture of lightsheet datasets, and reviewed the manuscript. CK designed and performed all computational modelling experiments, performed data analysis, and reviewed the manuscript. VS and AP designed and created all fluorescent *P. hawaiensis* constructs, performed embryo collection and injection experiments for capture of lightsheet datasets, and reviewed the manuscript. CGE conceived of the study, performed data interpretation, obtained funding for the study, supervised its execution, and edited the manuscript.

Funding
This work was supported by a National Science Foundation (NSF) Graduate Student Research Fellowship 2018259071 and a Simmons Award from the Harvard Center for Biological Imaging to BLS, NSF award IOS-2220747 to CGE, the NSF-Simons Center for Mathematical and Statistical Analysis of Biology at Harvard (award number DMS-1764269) and the Harvard Quantitative Biology Initiative (CK) and funds from the Howard Hughes Medical Institute (HHMI) and Harvard University. CGE is an HHMI Investigator.

Conflicts of Interest
The authors declare no conflicts of interest.

Data Availability
Lightsheet datasets described in Supplementary Table 1. MaMuT lineage tracks for these datasets, as well as scripts for cellular potts model simulations and image analyses, are available at https://github.com/boyonpointe/parhyale_morpho/tree/main with commit ID a19a88d.

Statement on Use of Machine Learning, Artificial Intelligence and Large Language Models
ChatGPT 4.0 and 5.0 (open AI) were used to modify R code for altering plot aesthetics. ilastik[101] and Cellpose[104], used for image segmentation in this study, are machine learning-based programs. ML/AI was not used to generate any content, write any text, or perform any other data analysis.

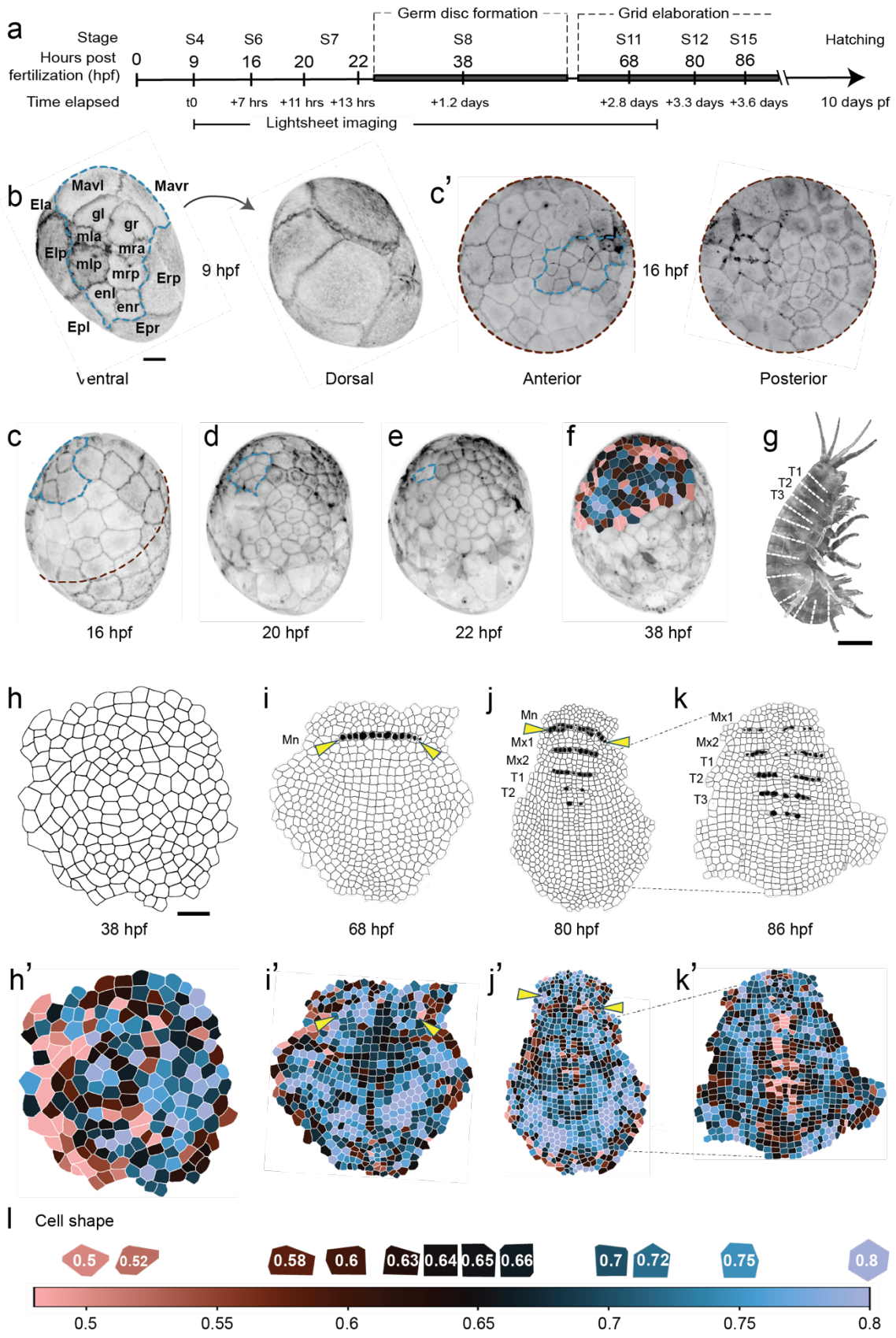
a
Germ disc formation
Grid elaboration
Stage
S4
S6
S7
S8
S11
S12
S15
Hatching
Hours post fertilization (hpf)
0
9
16
20
22
38
68
80
86
Time elapsed
t0
+7 hrs
+11 hrs
+13 hrs
+1.2 days
+2.8 days
+3.3 days
+3.6 days
10 days pf
Lightsheet imaging
b
Mavl
Mavr
Ela
gl
gr
mla
mra
Elp
mlp
mrp
Erp
enl
enr
Epl
Epr
9 hpf
Ventral
Dorsal
c'
16 hpf
Anterior
Posterior
c
d
e
f
g
T1
T2
T3
16 hpf
20 hpf
22 hpf
38 hpf
h
i
j
k
Mn
Mx1
Mx2
T1
T2
T3
38 hpf
68 hpf
80 hpf
86 hpf
h'
i'
j'
k'
l
Cell shape
0.5
0.52
0.58
0.6
0.63
0.64
0.65
0.66
0.7
0.72
0.75
0.8
0.5
0.55
0.6
0.65
0.7
0.75
0.8

Figure 1 (previous page). Formation of a cellular square grid in the *Parhyale hawaiensis* embryonic ectoderm. a Developmental timeline from fertilization to the hatching of juveniles with the window of lightsheet microscope imaging indicated at the bottom. Stages according to Browne and colleagues[29]. **b-f** Stills selected from a time-lapse of the first 1.5 days of development in a *P. hawaiensis* embryo that was live-imaged with a multiview lightsheet microscope; cell membranes marked with *Lyn-EGFP*. Micrographs are maximum intensity projections of a volume constructed by fusing 3D image stacks from all imaging angles, and are displayed either from a fixed perspective (b-f) or as conformal surface maps (c'). **b** Ventral (left) and dorsal (right) views of the 16-cell stage. The first cell divisions in *P. hawaiensis* are highly stereotypic and segregate the germ layers and germ line (gl and gr) by this stage. The eight micromeres and two macromeres enclosed within the blue dotted line are the mesoderm (ml, mr, Mav), endoderm (en), and germ-line (g) precursors, the descendants of which delaminate from the surface during gastrulation (c-e) leaving the at surface a continuous sheet of epithelial ectoderm (f). The remaining six macromeres (Epr, Epl, Era, Erp, Ela, Elp) will give rise to all ectodermal cells. **c-e** From approximately 16-22 hours post fertilization (hpf), cells begin reducing in size and migrate to the anterior pole, condensing into a germ disc (embryonic rudiment) sitting atop larger yolk-filled cells. **c'** Anterior (left) and posterior (right) conformal maps of the same image volume displayed in c. These 2D surface projections allow for simultaneous visualization of cell shapes and relationships that make up the embryo's curved surface. The maroon dotted line in c corresponds to those along map edges in c'. **f** By approximately 38 hpf, the surface of the germ disc is an epithelium made up entirely of ectoderm (colored cells). **g** An adult female *P. hawaiensis.* White lines indicate parasegmental boundaries with corresponding morphological segment identities. **h-k** Time series of fixed embryos in which the ectoderm was dissected away from the yolk and physically flattened to make surface cell geometries visible. A grid of square cells emerges within the expanding germ disc with the transition from hexagonal to square cells (**h'-k'**) progressing from anterior to posterior and laterally left and right (**i**). A row of cells expressing the segmentation gene *engrailed* appears in the prospective mandibular segment (Mn) around 68 hpf (arrowheads). **j, k** From 80 hpf onwards, progressing from anterior to posterior, nuclear-localized Engrailed protein is detectable in cells of the anterior-most cell row in each parasegment as it is generated via row-duplicating cell divisions from the midline to lateral regions. Dotted lines in j indicate the region of the embryo displayed in k. **l** Cell shape descriptor used to analyze square grid morphogenesis in this study. Mx1: first maxillary segment; Mx2: second maxillary segment; T1: first trunk segment; T2: second trunk segment; T3: third trunk segment.

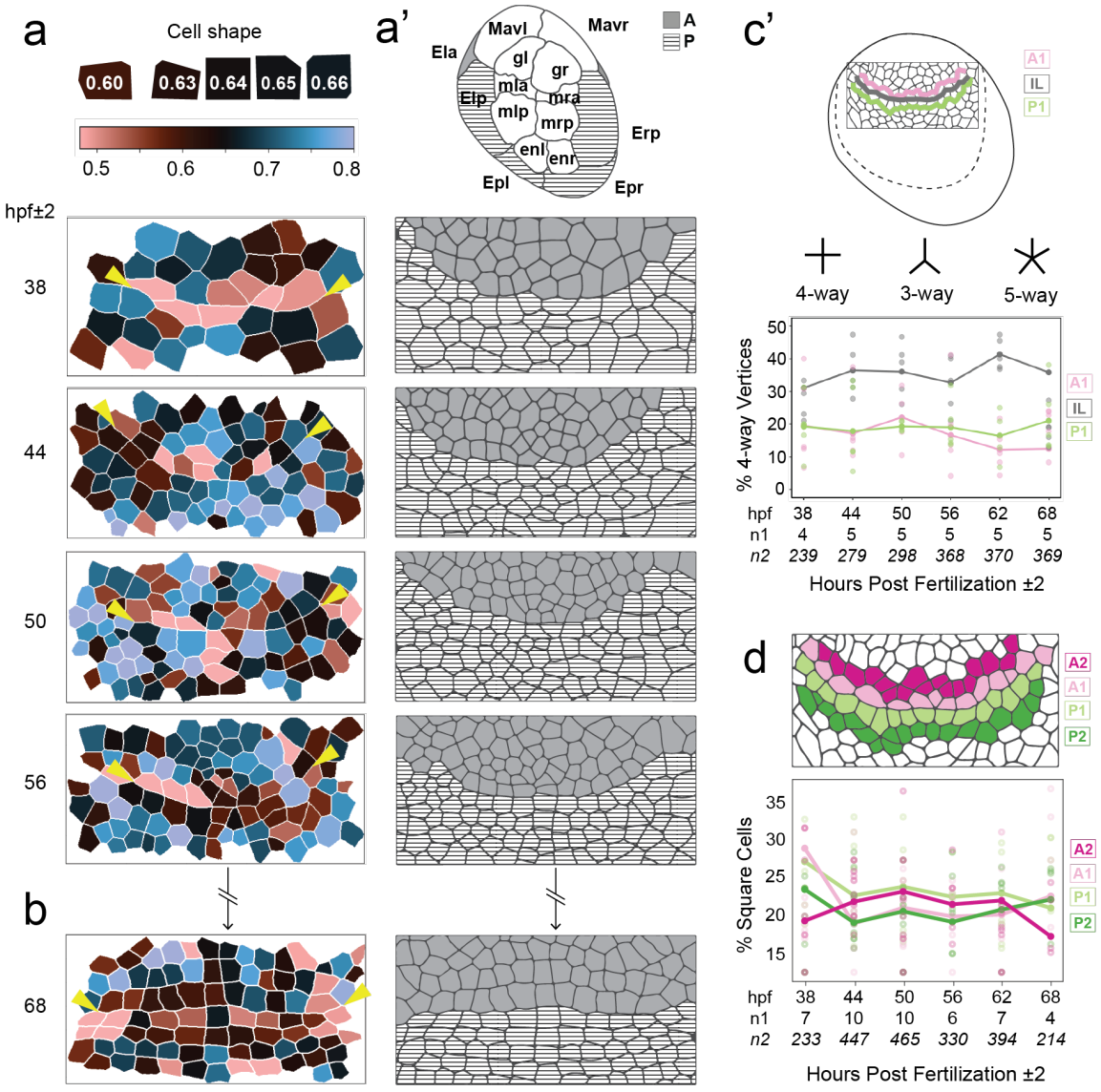

Figure 2. Square cell geometry initiates along the dorso-ventral axis at the initiation line, which is an ectodermal lineage compartment boundary. a-b 38-68±2 hpf manually flattened germ disks segmented to identify cell membranes, with cells colored according to their shape descriptor value. What we call the "initiation line" (IL; arrowheads in the left column), corresponds to the boundary of the anterior (A: grey) and posterior (P: striped) lineage compartments shown in a'. **a'** Stills from a lightsheet time-lapse that were conformally mapped onto 2D, showing descendants of ectodermal precursor macromeres (grey: anterior ectoderm founders Era, Ela; striped: posterior ectoderm founders Erp, Elp, Epr, Epl) The boundary between anterior and posterior clones begins as a jagged curve at 38±2 hpf and straightens out by 68±2 hpf. **c** Top: Schematic shows the analysed region (box) within the germ disk (dotted line). Bottom: Percentage of 4-way vertices at the IL (gray), the equivalent line one cell anterior (A1, light pink), and one cell posterior (P1, light green). **d** Top: Cell rows analyzed in in four different locations relative to the IL: immediately adjacent to the IL to the anterior (A1: light pink), immediately adjacent to the IL to the posterior (P1: light green), one cell diameter anterior to the IL (A2: dark pink) and one cell diameter posterior to the IL (P2: dark green). Bottom: plot showing percentage of square cells (shape descriptor value ⩾ 0.60 or ⩽0.66). Anterior is up in all images. Sample sizes in c and d indicated by n1: number of embryos and n2: number of vertices.

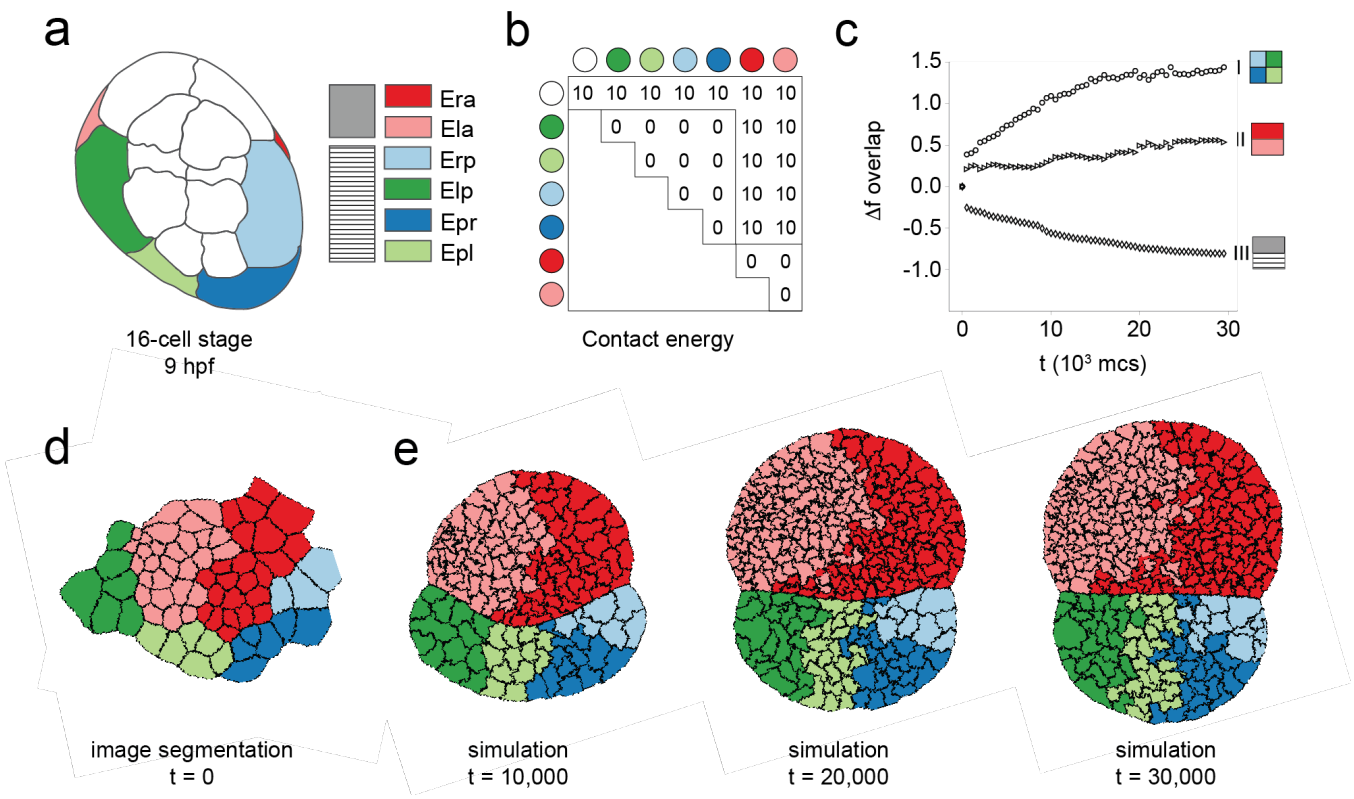

Figure 3. A simulation of cell sorting can explain the emergence of a straight boundary at the initiation line. a Tracing of a 16-cell stage embryo with the six ectodermal lineages colored. Grey and striped legend is provided to show the correspondence of these blastomere lineages to the anterior and posterior compartments shown in Figure 2. **b** Simulation contact energy inputs for each combination of lineage precursors (colored circles show blastomere identities as defined in a) as well as the environment surrounding the tissue (white circles). Higher contact energy results in decreased affinity between cells. **c** Change in normalized area of overlap plotted against time in Monte Carlo steps (mcs) for n = 10 runs of the simulation. Group I (circles) = boundaries among the four posterior lineages (Erp, Elp, Epr, Epl); group II (triangles) = boundary between the two anterior lineages (Era, Ela); group III (diamonds) = boundary between the anterior and posterior lineages. **d** Membrane segmentation of part of the conformally mapped germ disk of Embryo 1 (Supplementary Table 1) at 26 hpf. At this stage, gastrulation has already taken place, and the surface of the embryo is a continuous sheet of ectoderm. This segmentation was seeded as the starting point for the simulation. **e** Stills from three time points of the simulation of cell sorting among the 16-cell stage ectodermal lineages implemented in CompuCell3D with time denoted in arbitrary units. Cell division rates for each lineage from one of the lightsheet datasets were input into the model. Anterior is up in all embryo image panels.

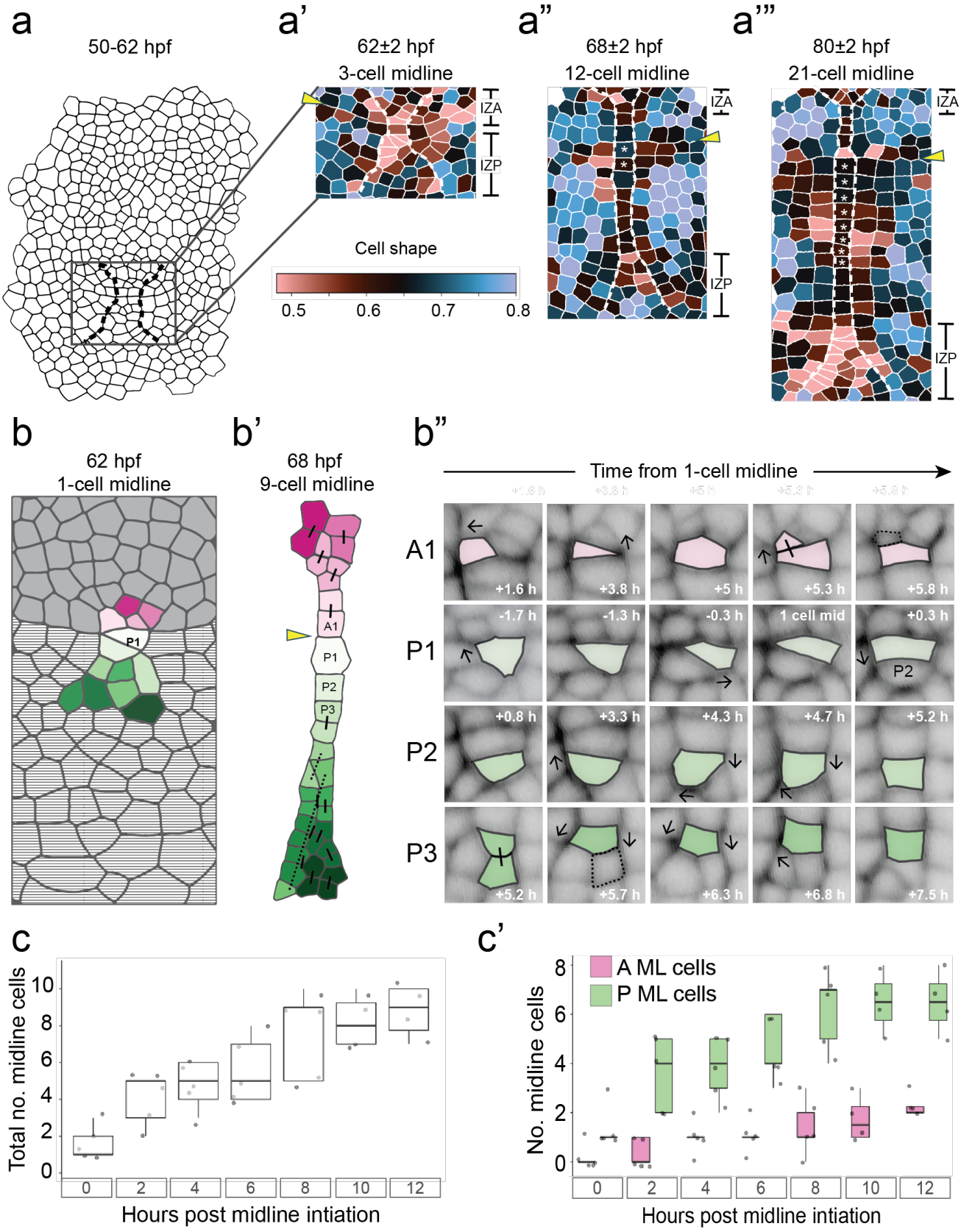
a
50-62 hpf
a'
62±2 hpf
3-cell midline
a"
68±2 hpf
12-cell midline
a'''
80±2 hpf
21-cell midline
IZA
IZP
Cell shape
0.5
0.6
0.7
0.8
b
62 hpf
1-cell midline
P1
b'
68 hpf
9-cell midline
A1
P1
P2
P3
b"
Time from 1-cell midline
A1
P1
P2
P3
+1.6 h
+3.8 h
+5 h
+5.3 h
+5.8 h
-1.7 h
-1.3 h
-0.3 h
1 cell mid
+0.3 h
+0.8 h
+3.3 h
+4.3 h
+4.7 h
+5.2 h
+5.7 h
+6.3 h
+6.8 h
+7.5 h
c
Total no. midline cells
Hours post midline intiation
c'
A ML cells
P ML cells
No. midline cells
Hours post midline intiation

798

Figure 4 (previous page). The secondary grid axis emerges as a column of square cells via the intercalation of a polyclonal founder cell population. a At 52-62 hpf, primarily anisotropic ectodermal cells near the ventral midline and spanning the IL (arrowheads in a', a", a'"), in a region we denote the intercalation zone (IZ), intercalate simultaneously in the anterior and posterior directions to form a single column of square cells forming the midline of the embryo (**a'**). **a"** The cells within the midline are the first cells to become square. Cells flanking the midline on the left and right then adopt square shapes posterior to the IL. Cells in a', a", and a'" are colored according to the cell shape descriptor. * in a" and a"' indicates midline cells that have undergone parasegment precursor row duplication. **b** Cells that join the midline derive from a polyclone of founder cells that span the anterior (grey)-posterior (stripes) compartment boundary (arrowhead). **b'** Founder cells intercalate in both anterior (IZA) and posterior (IZP) intercalation zones (as shown in a', a" and a'"), adding or subtracting sides until they form a square. Arrows indicate the direction of a growing or shrinking cell side. Dotted outlines in rightmost panel of top row and second panel of bottom row indicate the outlines of the sister cell resulting from the division in the previous panel. **c** Numbers of total cells in the midline over time (n = 5 embryos). Midline initiation is defined as the time when the first posterior cell (P1) is aligned. By 12 hours after midline initiation, a mean of nine total cells have been added to the midline. **c'** Numbers of cells in the midline anterior (A ML: pink) and posterior (P ML: green) to the IL over time (in = 5 embryos). Anterior is up in a-a"' and b-b''.

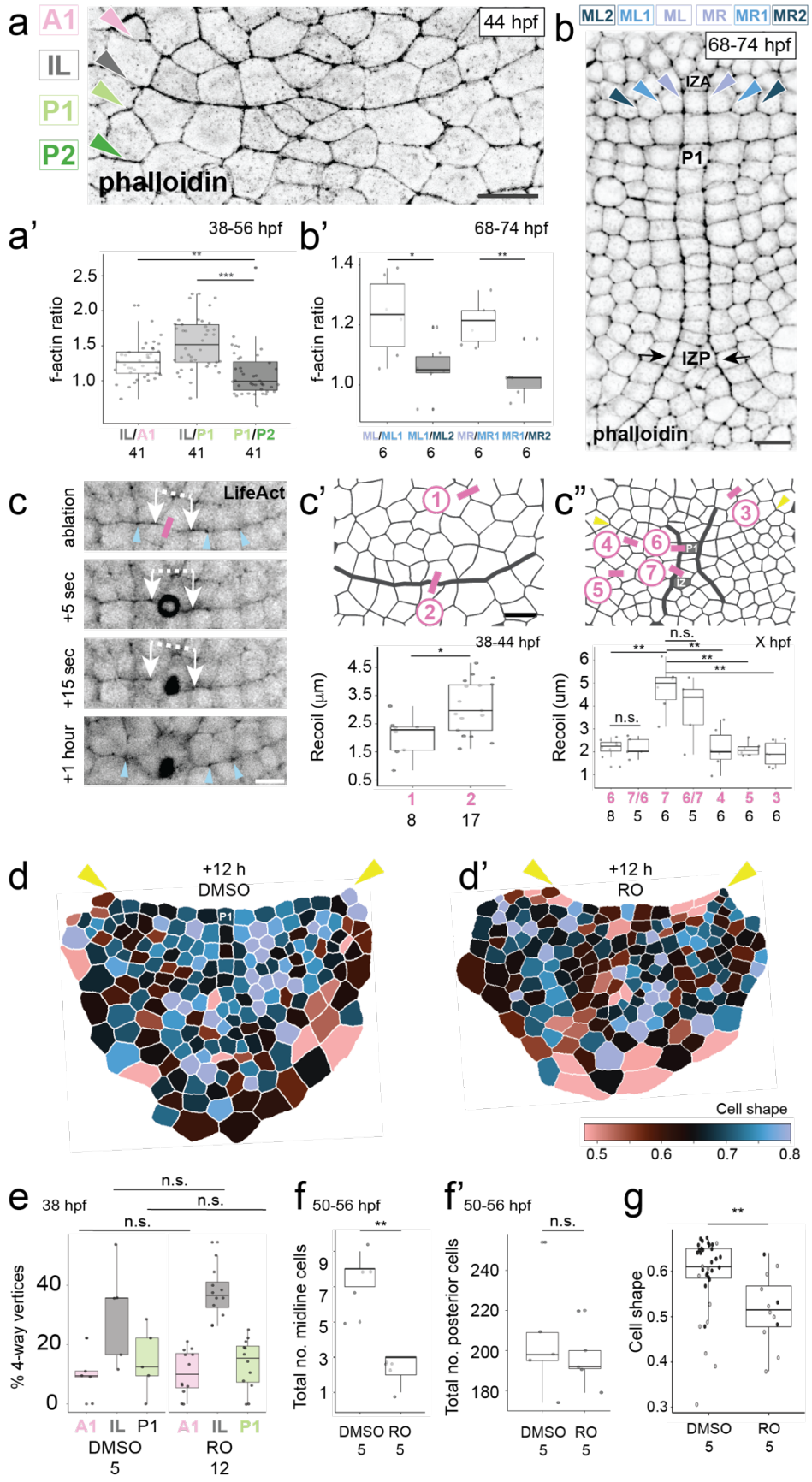
a
A1
IL
P1
P2
44 hpf
phalloidin
b
ML2 ML1 ML MR MR1 MR2
68-74 hpf
IZA
P1
IZP
phalloidin
a'
38-56 hpf
f-actin ratio
IL/A1 IL/P1 P1/P2
41 41 41
b'
68-74 hpf
f-actin ratio
ML/ML1 ML1/ML2 MR/MR1 MR1/MR2
6 6 6 6
c
LifeAct
ablation
+5 sec
+15 sec
+1 hour
c'
38-44 hpf
Recoil (μm)
1 2
8 17
c''
X hpf
n.s.
Recoil (um)
6 7/6 7 6/7 4 5 3
8 5 6 5 6 6 6
d
+12 h
DMSO
P1
d'
+12 h
RO
Cell shape
0.5 0.6 0.7 0.8
e
38 hpf
n.s.
% 4-way vertices
A1 IL P1 A1 IL P1
DMSO RO
5 12
f
50-56 hpf
Total no. midline cells
DMSO RO
5 5
f'
50-56 hpf
n.s.
Total no. posterior cells
DMSO RO
5 5
g
Cell shape
DMSO RO
5 5

816

Figure 5 (previous page). The initiation line and midline borders are tensile cytoskeletal cables. a Maximum intensity projection of 20 0.5µm optical sections of the ventral ectoderm of a 44±2 hpf embryo stained with phalloidin to label f-actin. **a'** Ratios of mean f-actin intensity measured in 38-56 hpf embryos. The regions quantified (A1, IL, P1, P2) are shown in **a**. Each region begins at the arrowhead on the right of the micrograph and extends across approximately 10 contiguous cell sides to the left side of the micrograph. **b** Maximum intensity projection of six 0.9µm optical sections of a 68-74 hpf embryo with a 15-cell midline; f-actin is labeled with phalloidin as in a. Arrowheads indicate the six regions (lines running parallel to the anterior-posterior axis, named MR, MR1, MR2, ML, ML1, ML2) where f-actin intensity was quantified. Each region quantified begins at the arrowhead shown in **b** and extends towards the posterior along contiguous cell sides to the posterior IZ (black arrows). **b'** Ratios of mean f-actin intensity measured in 68-74 hpf embryos with 7-15-cells in the midline. **c** 38-44 hpf embryo subject to laser ablation at the IL. **c** Pink rectangle indicates the ablation site; white arrows connected by a dashed line indicate the lengths measured to calculate recoil; blue arrowheads at IL indicate vertices surrounding the incision site. **c'** Ablation sites (top: thick line indicates the IL) and recoil plot (bottom) in 38-44 hpf embryos in which recoil was measured following IL ablation. **c"** Ablation sites (top: thick lines indicate the cables demarcating the nascent midline) and recoil plot (bottom) in 58-69 hpf embryos with 3-7 cells in the midline. Pink numbers on X-axis categories indicate the ablation site as shown in the schematic above. 7/6 indicates that a first incision was made at position 6 (next to the midline P1 cell/at the compartment boundary), followed by a second incision at position 7 (posterior IZ). In 6/7, the same two incisions were made in reverse order. **d** 1-cell midline embryos (50-56 hpf) were incubated in 50µM DMSO or Rockout (**d'**), and the cells of the posterior compartment were segmented and their cell shape descriptor was color-mapped 12 hours later. The IL is indicated by yellow arrowheads. **e** Percentage of 4-way vertices in 38 hpf embryos incubated in DMSO and 50µM Rockout for 12 hours. P-values for comparisons between DMSO and RO-treated samples as follows: A1: 0.48; IL: 0.18; P1: 0.48. **f** Total number of midline cells is significantly decreased in 62-68 hpf embryos treated with Rockout for 12 hours (p-value = 0.004). **f'** Total number of cells in the posterior compartment of 62-68 hpf embryos treated with Rockout for 12 hours is not significantly different from DMSO controls (p-value = 0.35). **g** Cell shape values for cells aligned into the midline in 12-hour DMSO (n = 35 cells) and Rockout (n = 12 cells) treated embryos. Grey symbols indicate the single cells at the anterior-most and posterior-most positions of the midline; black symbols indicate all other midline cells. Samples are the same as those plotted in f and f' (p-value = 0.002). * p-value < 0.05; ** p-value < 0.01; *** p-value < 0.001; n.s. not significant (Mann Whitney U-test; all tests one-tailed). Scale bars for a, c', d = 25µm and c = 15µm. Anterior is up in all micrographs. Sample sizes (number of embryos) in all plots indicated by numbers underneath category labels.

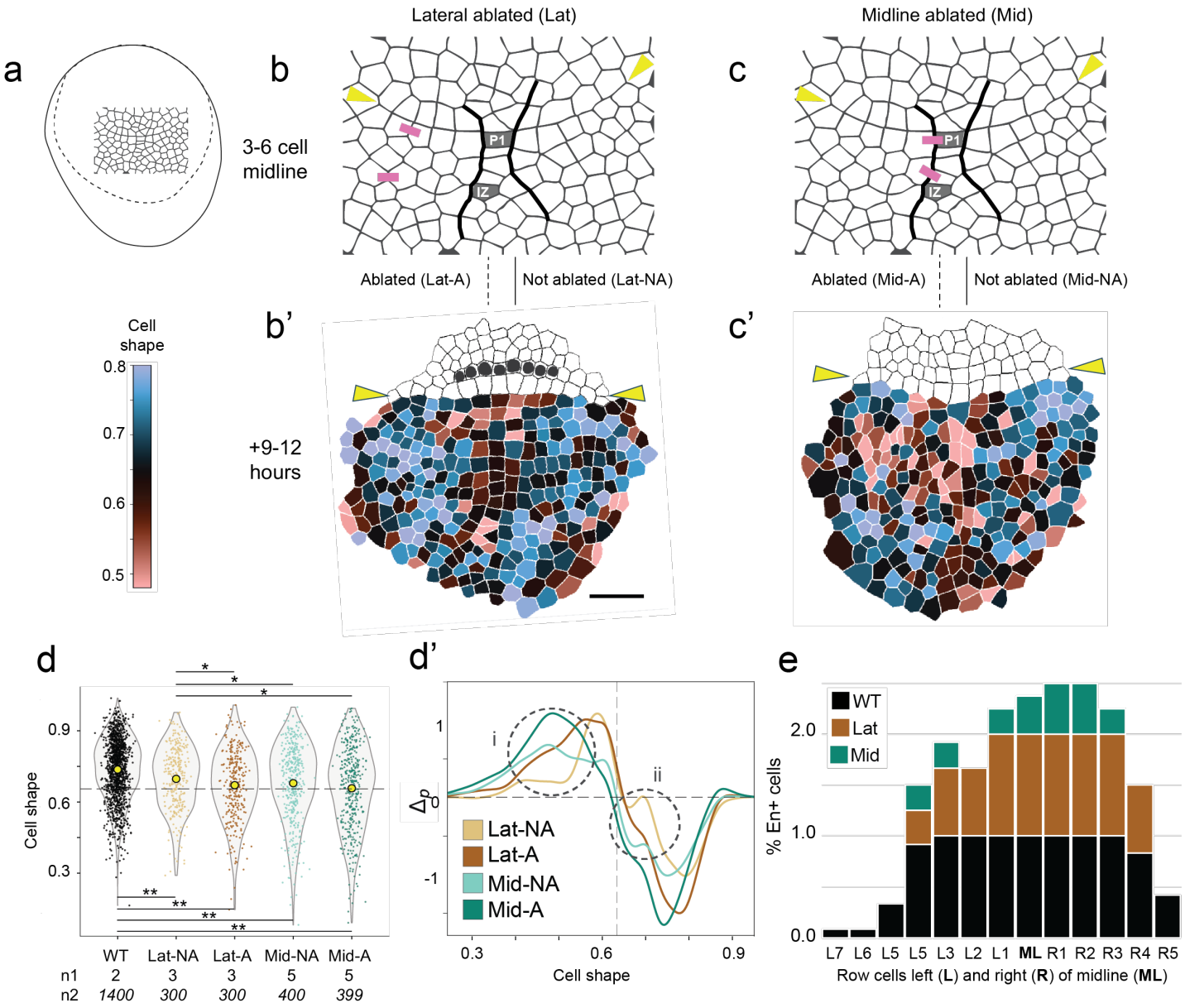
a
b
Lateral ablated (Lat)
3-6 cell midline
P1
IZ
Ablated (Lat-A)
Not ablated (Lat-NA)
c
Midline ablated (Mid)
Ablated (Mid-A)
Not ablated (Mid-NA)
Cell shape
0.8
0.7
0.6
0.5
b'
+9-12 hours
c'
d
Cell shape
0.9
0.6
0.3
WT
Lat-NA
Lat-A
Mid-NA
Mid-A
n1 2 3 3 5 5
n2 1400 300 300 400 399
d'
i
ii
Δp
1
0
-1
Lat-NA
Lat-A
Mid-NA
Mid-A
0.3
0.6
0.9
Cell shape
e
WT
Lat
Mid
% En+ cells
2.0
1.0
0.0
L7 L6 L5 L5 L3 L2 L1 ML R1 R2 R3 R4 R5
Row cells left (L) and right (R) of midline (ML)

850

Figure 6 (previous page). The midline cables organize square-cell packing and the emergence of the first complete stripe of Engrailed-positive nuclei. a The region within the germ disc where ablations were made, delineated by the dotted line. **b, c** Locations of laser ablations performed in different regions of the ventral epithelium in 58-69 hpf embryos with 3 – 6 cells in the midline. **b', c'** Cell shape descriptor values and En expression 9-12 hours after ablation. **d** Cell shape descriptor value distributions across treatments, including unablated embryos (WT) of equivalent chronological age. Yellow circles indicate the mean, dotted line the value for an isometric square. Only significantly different pairwise comparisons (based on the bootstrapping approach described in Methods) are indicated as follows: * $p < 0.05$; ** $p < 0.01$. Sample sizes indicated by n1: number of embryos and n2: number of cells. **d'** Deviation of the four ablated groups from the WT probability density ($\Delta_p = 0$) over the range of cell shape values observed. A positive value indicates shapes gained and a negative value indicates shapes lost. Dotted vertical line indicates the value for an isometric square; colors are the same as in panel d. **e** Proportion of Mn cells (categories on horizontal axis) expressing En in wild type and in embryos subjected to lateral (brown) or midline (green) ablations shown in b and c respectively. Data in Supplemental Table 3.

Movie Legends

Movie 1. **The first 2.5 days of development of a membrane-labeled *P. hawaiensis* embryo**. Timelapse animation of the *Lyn-GFP* (membrane) channel of a reconstructed multiview lightsheet dataset beginning at the 8-cell stage and ending during germ band grid elaboration. Each frame is a maximum intensity projection through half of the embryo and was taken ten minutes apart. 319 total frames are animated at a frame-rate of nine frames per second. Sequential frames from this animation were selected for and sequentially displayed in Figure 1 (first frame is Fig. 1b).

Movie 2. **The first 2.5 days of development of a nuclear-labeled *P. hawaiensis* embryo**. Timelapse animation of the *H2A-mCherry* (nuclei) channel of the same embryo shown in Movie 1. Each frame is a maximum intensity projection through half of the embryo and was taken ten minutes apart. 319 total frames are animated at a frame-rate of nine frames per second.

Movie 3. **Dynamics of the 16-cell stage lineage domains visualized by stop-motion animation**. The left side of this animation shows a still from Movie 1 with the *Lyn-GPF* marked 16-cell stage ectodermal blastomeres false colored (Era = magenta, Ela = pink, Erp = yellow, Elp = purple, Erp = cyan, Elp = orange). The right side shows 2D maps of the same dataset in which the MaMuT nuclear tracks have been superimposed on the membrane channel to show the lineage of each cell. The rectangular cut-out corresponds to the cropped regions of each map shown in Fig. 2c, Fig. 6a, Supplementary Fig. 1 and Supplementary Fig. 8a. The maps shown here begin at 42 hpf and end at 55.67 hpf and are animated at a frame rate of nine frames per second, displaying 1.5 hours of developmental time every second. Given that the mapping of the 3D surface to 2D was not constrained and the germ disk migrates across the yolk, frames were manually aligned to produce animated motion and keep the emerging grid fixed within the cut-out region. The first sweep of the pointing finger across the map (00:07) indicates the IL (Fig. 2) at the anterior-posterior compartment boundary. The second sweep at the end (00:10) indicates the emerging midline (Fig. 4), which separates the Erp and Elp lineages by one cell beginning just posterior to the IL (P1 in Fig. 4b).

Movie 4. Intercalation of midline cells to form a column of square cells. The midline of the germ band grid forms as a single column of cells via intercalation. Cells aligned into the midline and within the intercalation zone at 66±2 hpf were tracked backwards to the onset of midline formation.

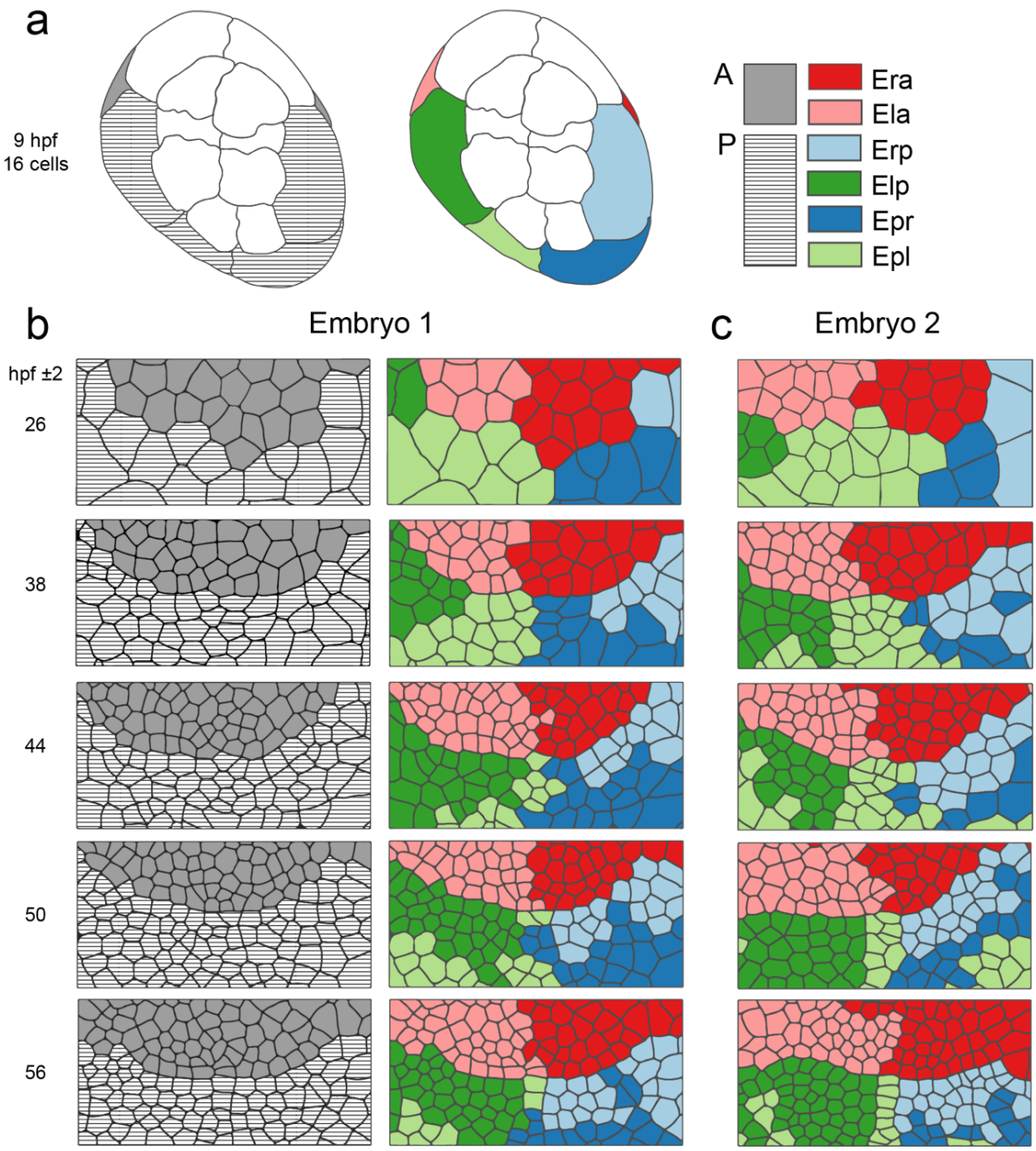

Supplementary Figure 1. 16-cell ectodermal lineage domains undergo extensive rearrangement. Stills from long-term multiview lightsheet timelapses shown either as tracings of maximum intensity projections (a) or 2D conformal maps (b-c) in which lineage was determined by tracking each cell back to its 16-cell stage ancestor. **a** 16-cell ectoderm precursor blastomere identities for Embryo 1 (Supplementary Table 1) colored with reference to anterior (grey)-posterior (striped) compartments or 16-cell stage identity (colors). **b-c** Lineage domain comparison between Embryo 1 and Embryo 2 (Supplementary Table 1) showing that in both embryos, anterior lineages (Era, Ela) do not mix with posterior lineages (Erp, Elp Epr, Epl). In the posterior compartment, the Erp and Elp domains begin on opposite (left and right) sides of the germ disk at 26±2 hpf and migrate closer to one another until they are separated by only a single column of Epr or Epl cells by 56±2 hpf, indicating the presence of extensive cell rearrangement.

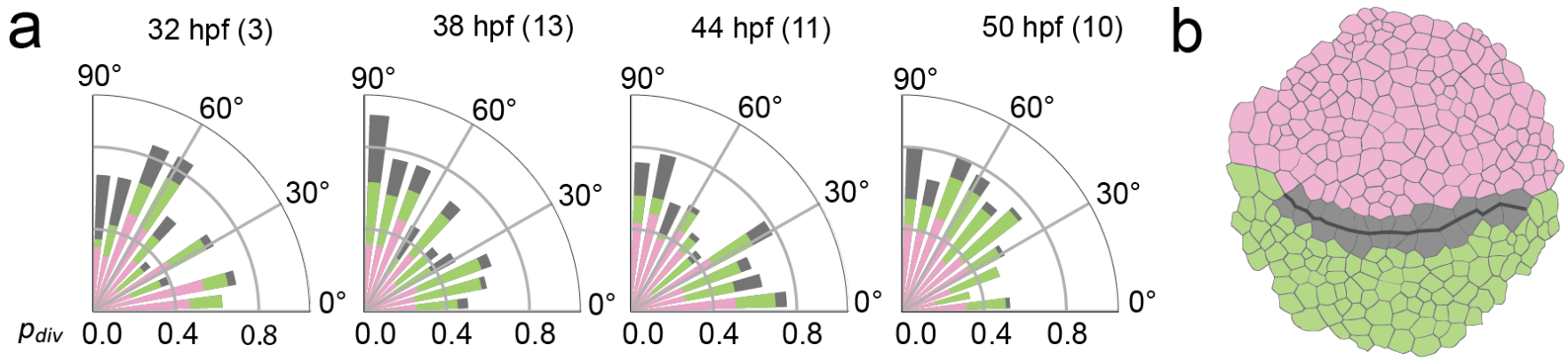

Supplementary Figure 2. Cell proliferation occurs throughout the germ disk from 32-30 hpf, with IL-adjacent divisions oriented preferentially perpendicular to the IL. a Cell division angles measured across the germ disc in 32-50 hpf embryos (sample size in parentheses). Angles are plotted with reference to the orientation of the IL (0°) and colored according to the division region (anterior = pink, IL = grey, posterior = green). **b** Segmented germ disk indicating locations of defined tissue regions. IL cell divisions are those that occur in cells directly adjacent to the IL on the anterior or posterior side (grey).

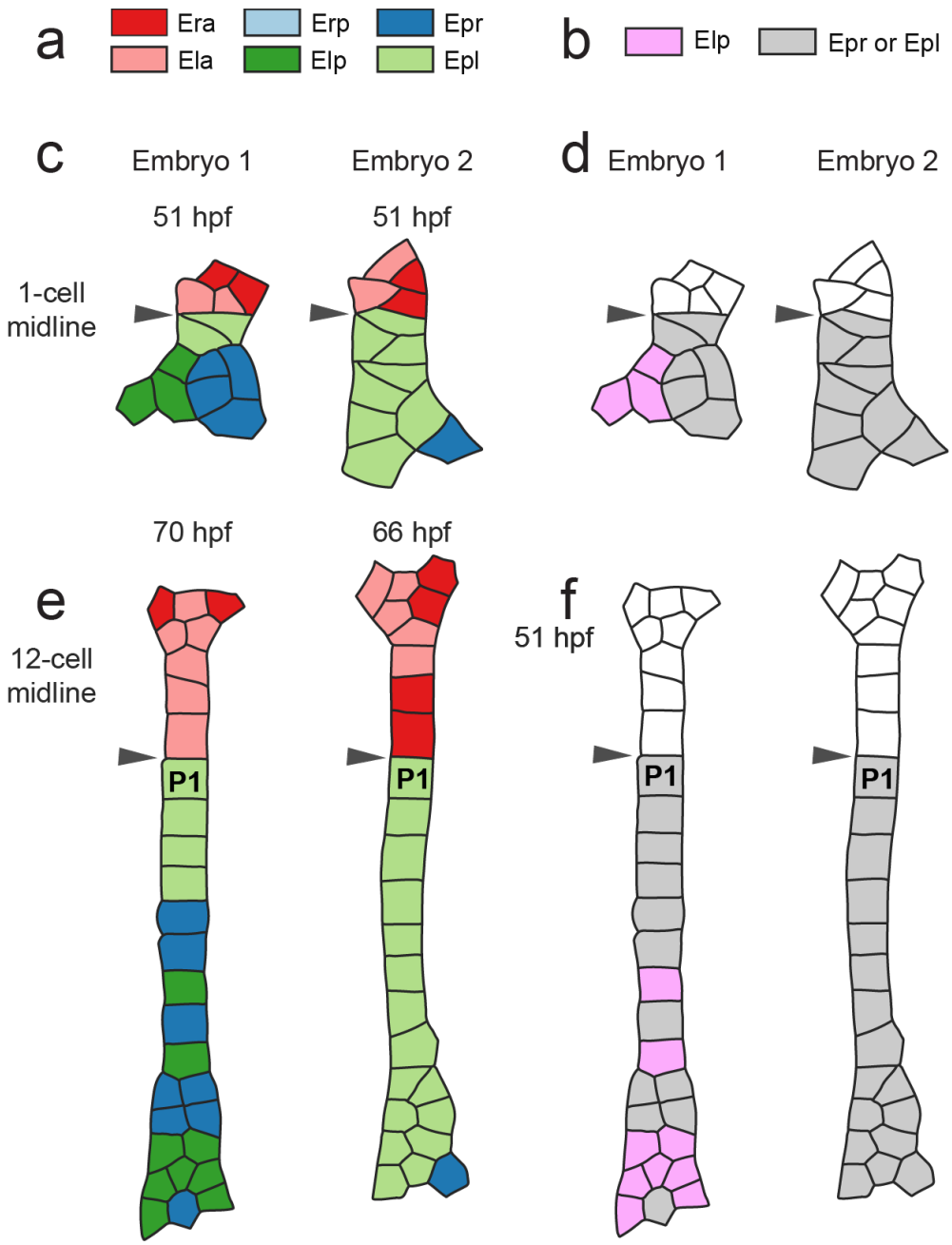

Supplementary Figure 3. Multiple 16-cell stage ectodermal lineages contribute to the midline, including non-Ep clones in the posterior. a Legend for 16-cell stage ectodermal precursor blastomeres. Midline descendants shown in c and e. **b** Legend for 16-cell stage Ep and non-Ep ectodermal precursor blastomeres. **c, e** The midline is composed of descendants of multiple 16-cell blastomeres both anterior and posterior to the anterior-posterior compartment boundary, which we call the IL at earlier stages. Midline cells in 12-cell midline embryos were tracked back to the 16-cell stage in the lightsheet datasets. At the 1-cell midline timepoint, only cells whose descendants make up the midline or intercalation zones shown in the 12-cell midline timepoints, are shown. **d, f** The posterior midline is not exclusively made up of descendants of Ep. Arrowheads indicate the location of the compartment boundary. In c through f, Embryos 1 and 2 correspond to the same datasets shown in Supplementary Figure 1 and described in Supplementary Table 1.

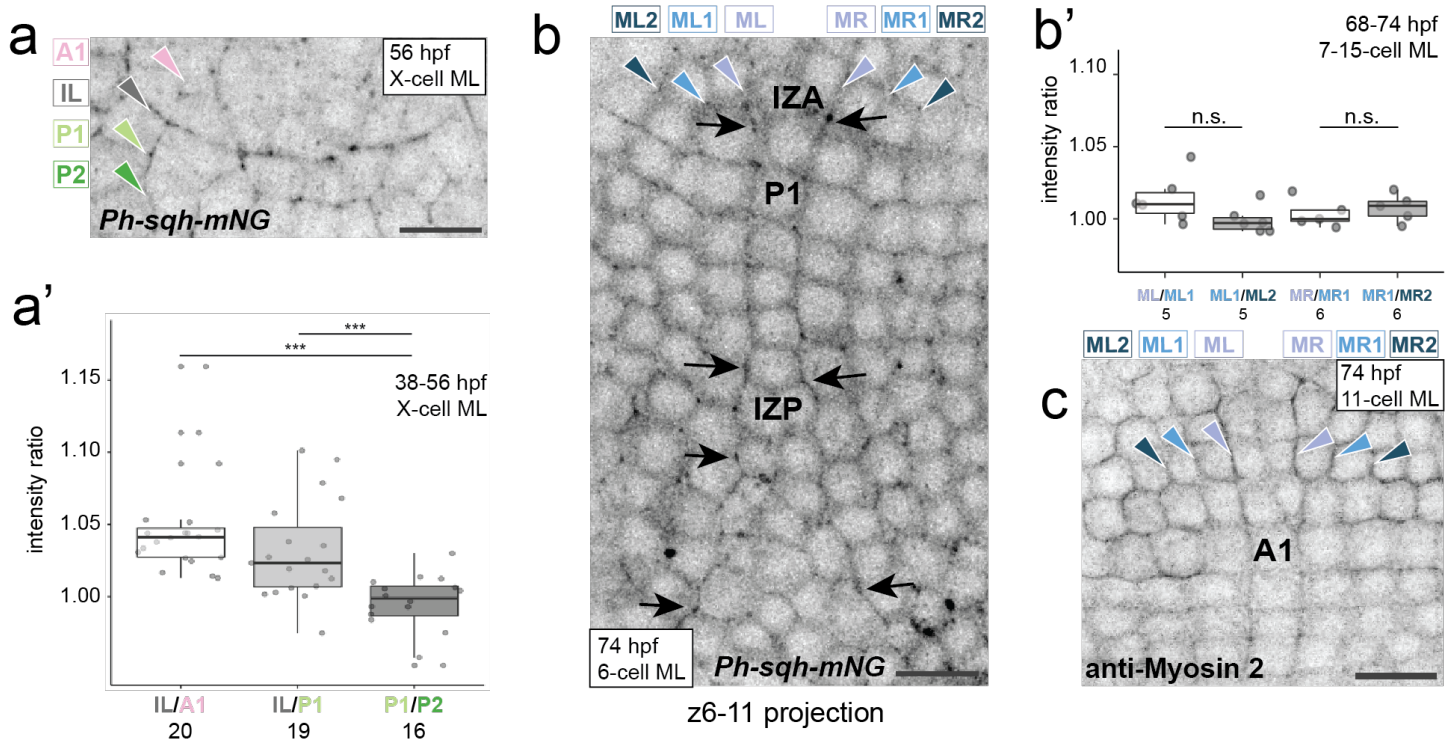

Supplementary Figure 4. Myosin 2 accumulates at the IL and midline cables. a 10µm maximum intensity projection of a 56±2 hpf embryo injected with *Ph-sqh-mNG* mRNA to label the myosin 2I regulatory light chain. **a'** Ratios of mean intensity of *Ph-sqh-mNG* signal measured from 38-56 hpf embryos in 10µm maximum intensity projections like that shown in a. The regions where *Ph-sqh* signal was quantified (A1, IL, P1, P2) are shown in a; each begins at the arrowhead and extends across contiguous cell sides to the rightmost edge of the region shown. **b** Maximum intensity projection through 5µm of a 74 hpf embryo at the 6-cell midline stage. Arrows indicate regions of myosin- 2 accumulation along the MR and ML cables (arrowheads), and at the anterior and posterior intercalation zones (IZ). **b'** Ratios of mean intensity of *Ph-sqh-mNG* signal measured from 5µm maximum intensity projections labeled with *Ph-sqh-mNG* expression . The regions quantified (MR, MR1, MR2, ML, ML1, ML2) are shown in b; each begins at the arrowhead and extends down contiguous cell sides to the bottom of the region shown. p = 0.05 for ML/ML1 compared to ML1/ML2; p = 0.20 for MR/MR1 compared to MR1/MR2. **c** 5µm maximum intensity projections of a 74 hpf embryo with 11 cells at the midline, labeled with an anti-Myosin 2 antibody. Only the anterior portion of the midline is shown here. Scale bars = 25µm and anterior is up in all micrographs. For all statistical comparisons * p-value < 0.05, ** p-value < 0.01, *** p-value < 0.001, and n.s. = not significant (Student's t-test for a; Mann Whitney U-test for b; all tests one-tailed). Sample sizes in a' and b' (numbers of embryos) indicated by numbers under category labels.

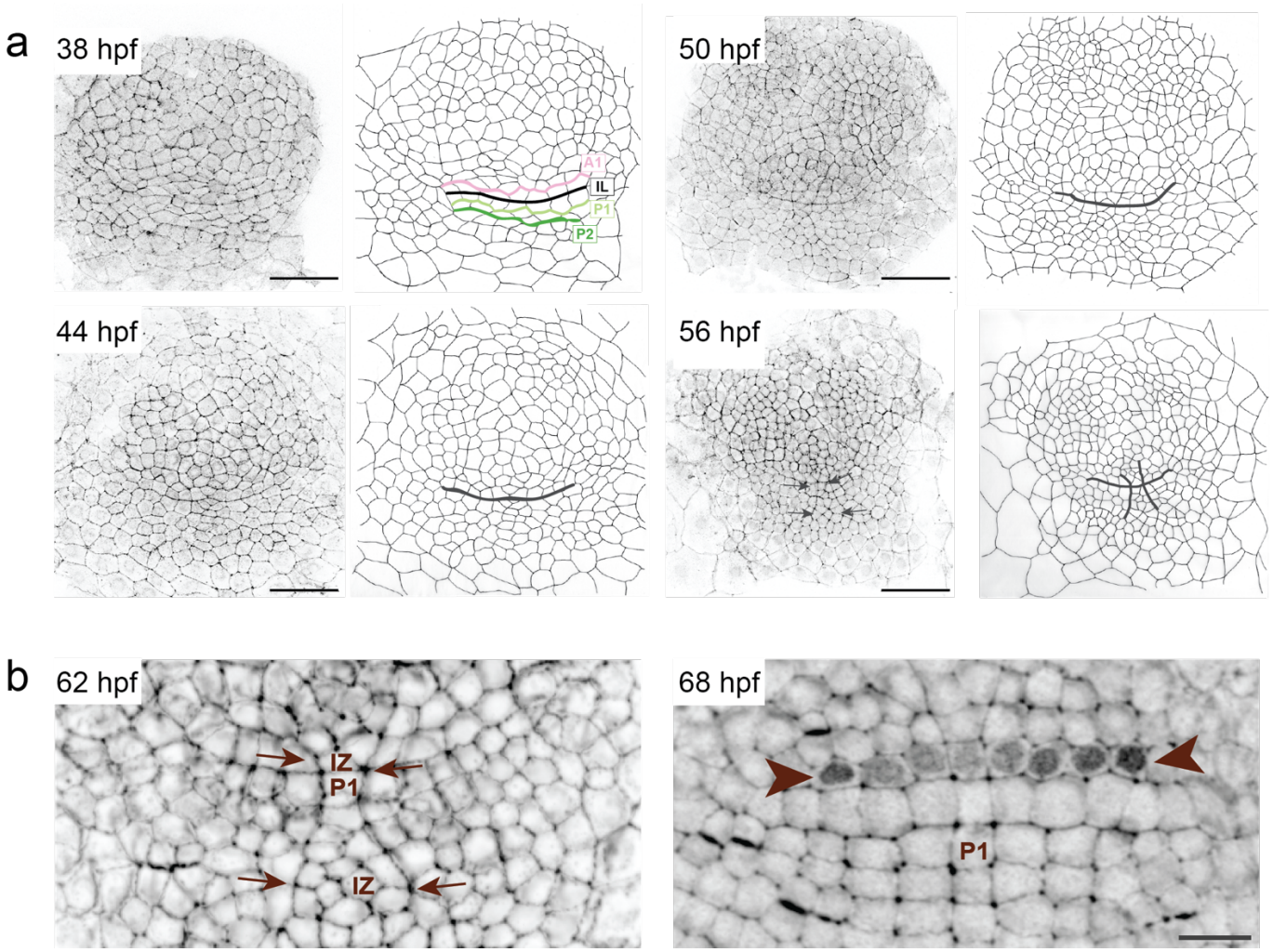

Supplementary Figure 5. IL and midline cables in the context of the whole germ disk. a 10µm maximum intensity projections of 38-56±2 hpf embryos stained with phalloidin (left) and with membranes traced (right). IL (all stages shown) and midline cables (56 hpf only) demarcated with thick lines. Anterior is up; scale bar = 100µm. **b** 10µm maximum intensity projections of the regions around the IL and midline cables in 62-68±2 hpf embryos. Arrows indicate the midline cables flanking the intercalation zone (IZ). Arrowheads indicate Engrailed expression in the prospective mandibular segment (Mn). Anterior is up; scale bar = 20µm.

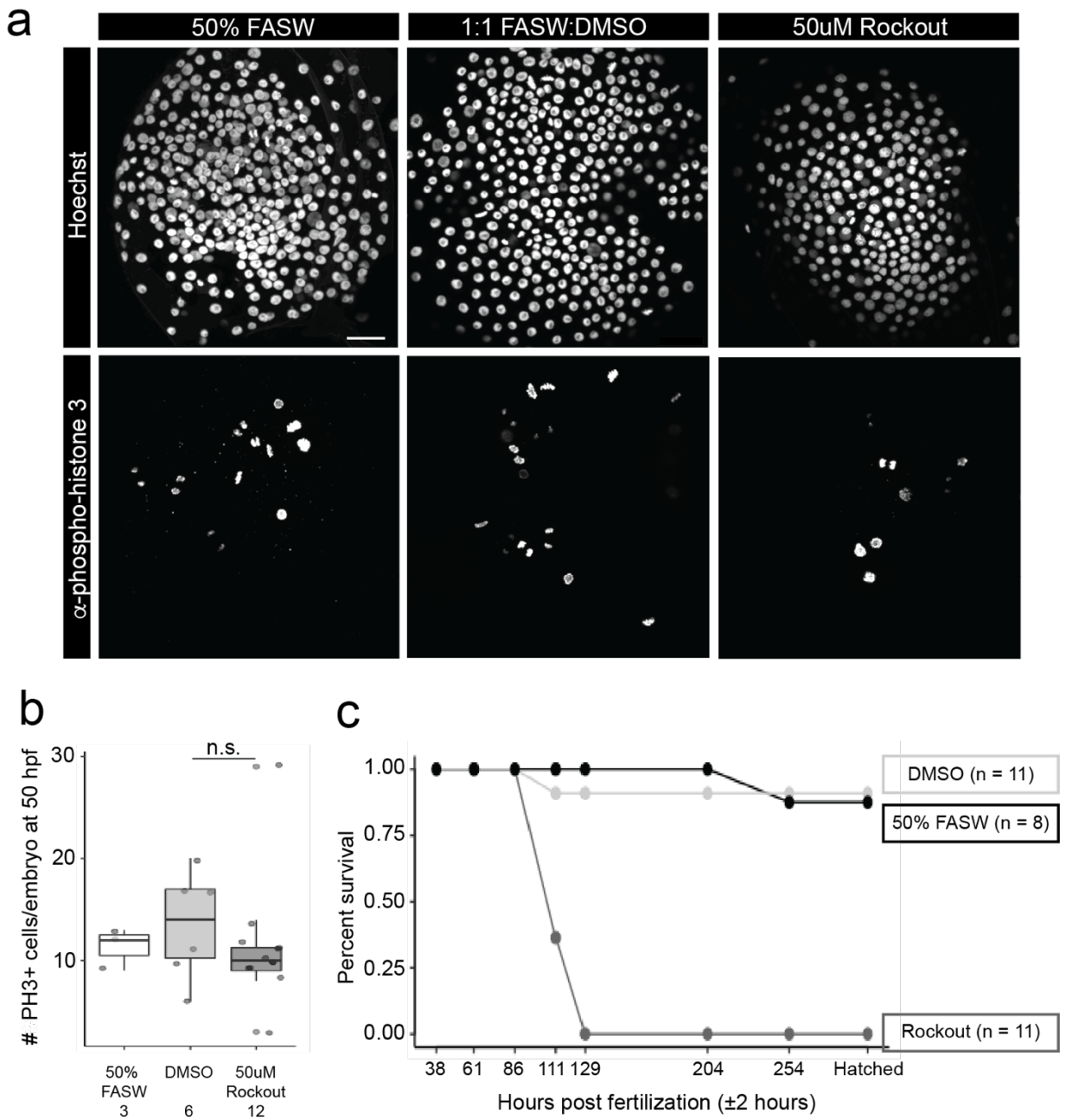

Supplementary Figure 6. 12-hour Rockout treatment does not impact cell proliferation. a 38±2 hpf embryos treated with either 50% FASW, 1:1 FASW:DMSO, or 50µM Rockout in 50% FASW were fixed 12 hours later (at 50±2 hpf), stained with Hoechst 33342 (top row) and anti-phospho-histone H3 (bottom row). Scale bar = 100µm and applies to all panels. **b** Total number of phospho-histone H3-positive cells for each treatment shown in a. n.s. = not significant (p-value = 0.303, two-tailed Mann-Whitney U Test). **c** Continuous treatment hatching assay. 100% of embryos incubated in 50µM Rockout continuously beginning at 38±2 hpf remained alive after 48 hours of treatment (86±2 hpf), and all died by 91 hours of treatment (129±2 hpf) (n = 11 embryos). By contrast, 100% of embryos in the 50% FASW (n = 8) and 1:1 FASW:DMSO (n = 11) treatments remained alive until 204±2 hpf. 87.5% hatched in 50% FASW and 90.1% of embryos hatched in 1:1 FASW:DMSO. Sample sizes in b indicated by numbers underneath category labels.

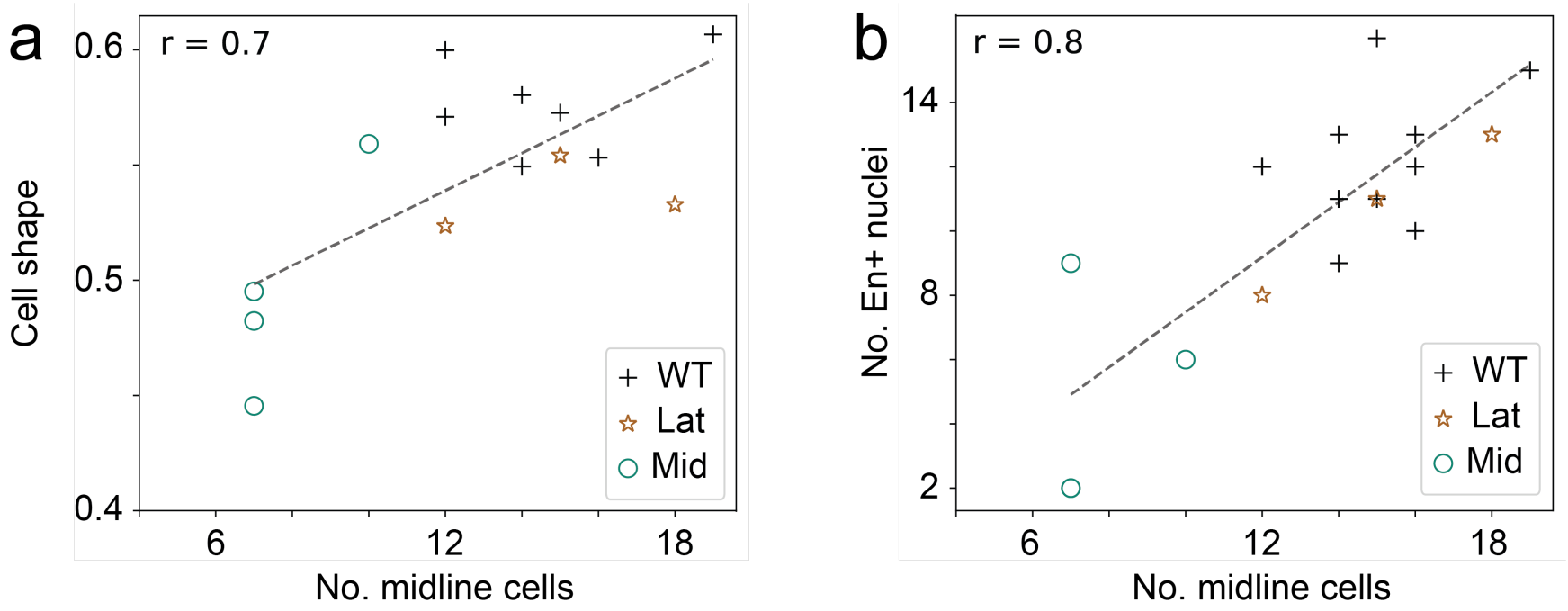

Supplementary Figure 7. a The bottom tenth percentile of the cell shape value (Fig. 1l) distribution of the whole tissue (i.e. the most anisotropic/least round cells) correlates positively with the total number of midline cells for that sample, in both wild type and ablated embryos. For wild type embryos, the roundness value of the bottom tenth percentile of cells is close to 0.6, implying that the shape of most non-round cells in wild type tissues is a square. However, upon midline ablation, the roundness value for this bottom tenth percentile is well below 0.6, implying that cells that would have been square in the wild type adopt more asymmetric shapes. The most dramatic impact on cell shape is experienced by the cells in the midline, which are approximately 10% of the cells in the tissue at this stage (data not shown). **b** The total number of Engrailed-positive (En+) nuclei correlates positively with the total number of midline cells.

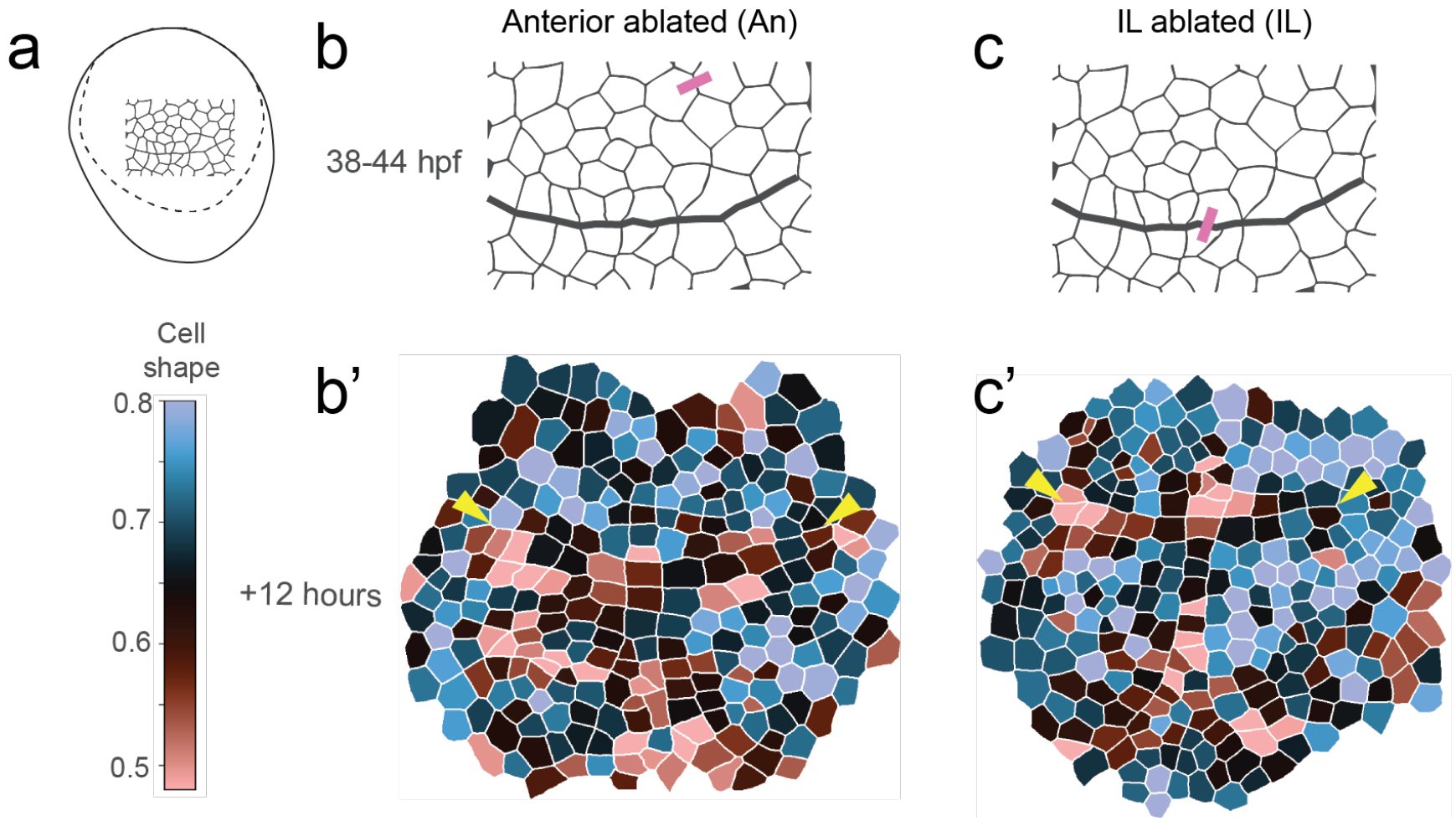

Supplementary Figure 8. Ablated IL embryos maintain a straight line at the IL and form a midline. a Schematic showing the location of the region delineated in b and c. **b** Ablation of a cell bond four cells anterior to the IL (n = 2). Ablation sites indicated by the pink rectangles. **b'** Cell shape descriptor values mapped on to +12 hour ablation tissue segmentations. **c** Ablation of a cell bond at the IL (n = 5). Ablation site indicated by the pink rectangle. **c'** Cell shape descriptor values mapped as described in b'. Arrowheads: IL.

988

Lightsheet Sample	Total imaging time (h)	T-interval (min)	16-cell lineages tracking	Midline tracking	Posterior cell numbers	Cell division orientation	Tissue morphology seeds for simulation
Embryo 1	61.00	10	Yes	Yes	Yes	Yes	Yes
Embryo 2	61.00	10	Yes	Yes	Yes	Yes	No
Embryo 3	66.33	10	No	Yes	Yes	Yes	No
Figure			**Fig. 2, Supp. Fig. 1**	**Fig. 4, Supp. Fig. 2**	**Fig. 5**	**Supp. Fig. 3**	**Fig. 3**

989

990 **Supplementary Table 1. Lightsheet datasets used for analyses.** h: hours. min: minutes.

991

					Live: 6hr time window				Fixed							
					Cell divisions in germ disk				Cell divisions in germ disk				Total cells in germ disk			
hpf	**N (live)**	**N (fixed)**	**N (total)**		**Total**	**A**	**IL**	**P**	**Total**	**A**	**IL**	**P**	**Total**	**A**	**IL**	**P**
32	3	0	3	Mean	54.33	31.33	9.67	13.33	4.67	3.33	1.33	0.00	154.00	84.00	16.67	53.33
				SD	17.16	14.05	4.04	1.53	1.53	2.31	1.53	0.00	18.19	14.93	1.15	13.65
				SE	9.91	8.11	2.33	0.88	0.88	1.33	0.88	0.00	10.50	8.62	0.67	7.88
38	3	10	13	Mean	69.33	30.33	13.00	26.00	5.42	2.67	1.00	1.92	238.92	155.33	20.62	64.31
				SD	8.50	5.13	4.58	1.73	2.11	1.61	1.00	1.04	23.60	20.72	2.10	7.97
				SE	2.36	1.42	1.27	0.48	0.58	0.45	0.28	0.29	6.55	5.75	0.58	2.21
				A vs P					0.10565				**<0.00001**			
44	2	10	12	Mean	108.50	66.00	16.00	26.50	5.45	2.91	0.75	1.75	311.91	183.64	24.33	103.83
				SD	21.92	7.07	8.49	6.36	2.62	2.07	0.75	1.36	31.23	19.30	2.57	25.56
				SE	6.33	2.04	2.45	1.84	0.76	0.60	0.22	0.39	9.02	5.57	0.74	7.38
				A vs P					0.09342				**0.00006**			
50	2	9	11	Mean	141.00	79.00	15.50	46.50	5.33	3.33	0.36	1.67	356.22	211.11	24.82	120.11
				SD	22.63	18.38	0.71	4.95	2.45	1.87	0.50	1.12	56.18	36.46	2.48	24.14
				SE	6.82	5.54	0.21	1.49	0.74	0.56	0.15	0.34	16.94	10.99	0.75	7.28
				A vs P					**0.03216**				**0.00029**			

Supplementary Table 2. Mitotic activity in the germ rudiment at the time of intercalation line (IL) formation. "Live" samples correspond to lightsheet sample embryos (Supplementary Table 1). Data from samples WT1, WT2 and WT3 were used to generate rose plots in Supplementary Figure 2a.

		Row cell identity																
Experiment	**Sample #**	**L7**	**L6**	**L5**	**L5**	**L3**	**L2**	**L1**	**ML**	**R1**	**R2**	**R3**	**R4**	**R5**	**R6**	**R7**	**Total # En+**	**Sample Mean**
Wild Type	**1**	0.00	0.00	0.00	1.00	1.00	1.00	1.00	1.00	1.00	1.00	1.00	1.00	0.00	0.00	0.00	9	0.60
	2	0.00	0.00	1.00	1.00	1.00	1.00	1.00	1.00	1.00	1.00	1.00	1.00	1.00	0.00	0.00	11	0.73
	3	0.00	0.00	1.00	1.00	1.00	1.00	1.00	1.00	1.00	1.00	1.00	1.00	1.00	0.00	0.00	11	0.73
	4	0.00	0.00	0.00	1.00	1.00	1.00	1.00	1.00	1.00	1.00	1.00	1.00	0.00	0.00	0.00	9	0.60
	5	0.00	0.00	1.00	1.00	1.00	1.00	1.00	1.00	1.00	1.00	1.00	1.00	1.00	0.00	0.00	11	0.73
	6	0.00	0.00	0.00	1.00	1.00	1.00	1.00	1.00	1.00	1.00	1.00	1.00	1.00	0.00	0.00	10	0.67
	7	0.00	0.00	0.00	1.00	1.00	1.00	1.00	1.00	1.00	1.00	1.00	1.00	0.00	0.00	0.00	9	0.60
	8	0.00	0.00	0.00	0.00	1.00	1.00	1.00	1.00	1.00	1.00	1.00	0.00	0.00	0.00	0.00	7	0.47
	9	0.00	0.00	0.00	1.00	1.00	1.00	1.00	1.00	1.00	1.00	1.00	1.00	0.00	0.00	0.00	9	0.60
	10	1.00	1.00	1.00	1.00	1.00	1.00	1.00	1.00	1.00	1.00	1.00	1.00	1.00	0.00	0.00	13	0.87
	11	0.00	0.00	0.00	1.00	1.00	1.00	1.00	1.00	1.00	1.00	1.00	1.00	0.00	0.00	0.00	9	0.60
	12	0.00	0.00	0.00	1.00	1.00	1.00	1.00	1.00	1.00	1.00	1.00	0.00	0.00	0.00	0.00	8	0.53
	Cell Mean	**0.08**	**0.08**	**0.33**	**0.92**	**1.00**	**1.00**	**1.00**	**1.00**	**1.00**	**1.00**	**1.00**	**0.83**	**0.42**	**0.00**	**0.00**	**9.67**	
Lateral Ablation	**1**	0.00	0.00	0.00	1.00	1.00	1.00	1.00	1.00	1.00	1.00	1.00	1.00	0.00	0.00	0.00	9	0.60
	2	0.00	0.00	0.00	0.00	1.00	1.00	1.00	1.00	1.00	1.00	1.00	1.00	0.00	0.00	0.00	8	0.53
	3	0.00	0.00	0.00	0.00	0.00	0.00	1.00	1.00	1.00	1.00	1.00	0.00	0.00	0.00	0.00	5	0.33
	Cell Mean	**0.00**	**0.00**	**0.00**	**0.33**	**0.67**	**0.67**	**1.00**	**1.00**	**1.00**	**1.00**	**1.00**	**0.67**	**0.00**	**0.00**	**0.00**	**7.33**	
Midline Ablation	**1**	0.00	0.00	0.00	1.00	1.00	0.00	1.00	1.00	1.00	1.00	0.00	0.00	0.00	0.00	0.00	6	0.40
	2	0.00	0.00	0.00	0.00	0.00	0.00	0.00	1.00	1.00	1.00	1.00	0.00	0.00	0.00	0.00	4	0.27
	3	0.00	0.00	0.00	0.00	0.00	0.00	0.00	0.00	0.00	0.00	0.00	0.00	0.00	0.00	0.00	0	0.00
	4	0.00	0.00	0.00	0.00	0.00	0.00	0.00	0.00	0.00	0.00	0.00	0.00	0.00	0.00	0.00	0	0.00
	Cell Mean	**0.00**	**0.00**	**0.00**	**0.25**	**0.25**	**0.00**	**0.25**	**0.50**	**0.50**	**0.50**	**0.25**	**0.00**	**0.00**	**0.00**	**0.00**	**2.50**	

Supplementary Table 3. En expression in cells of the prospective mandibular segment in wild type (WT) embryos, following ablation of cell bonds lateral to the midline (Lat), or following ablation of cell bonds at the midline, as depicted in Fig. 6b, c. These data were used to generate Fig. 6e.

References

1. His, W. *Untersuchungen über die erste Anlage des Wirbelthierleibes: die erste Entwickelung des Hühnchens im Ei*. (F.C.W. Vogel, Leipzig, 1868).

2. Keller, E. F. *The Century of the Gene*. (Harvard University Press, Cambridge, Mass., 2002).

3. Turing, A. M. The Chemical Basis of Morphogenesis. *Philos. Trans. R. Soc. Lond. Ser. B, Biol. Sci.* **237**, 37–72 (1952).

4. Neumann, C. & Cohen, S. Problems and paradigms: Morphogens and pattern formation. *BioEssays* **19**, 721–729 (1997).

5. Müller, G. B. & Newman, S. *Origination of Organismal Form: Beyond the Gene in Developmental and Evolutionary Biology*. vol. 2 (MIT Press, Cambridge, Mass, 2003).

6. Roeder, A. H. K. Arabidopsis sepals: A model system for the emergent process of morphogenesis. *Quant. plant Biol.* **2**, E14 (2021).

7. Gross, D., Sevrin, A. & Shraiman, B. The Physics of Living Matter: Space, Time and Information. in *Proceedings of the 27th Solvay Conference on Physics* (eds. Gross, D., Sevrin, A. & Shraiman, B.) (2020). doi:10.1142/10964.

8. Ghosh, S., Kuyyamudi, C., Steinert, B. L. & Extavour, C. G. Mechanical mechanisms of morphogenesis as potential substrates for evolutionary change. *Semin. Cell Dev. Biol.* **175**, 103645 (2025).

9. Caldarelli, P. *et al.* Self-organized tissue mechanics underlie embryonic regulation. *Nature* **633**, 887–894 (2024).

10. Stork, N. E. How Many Species of Insects and Other Terrestrial Arthropods Are There on Earth? *Annu. Rev. Entomol.* **63**, 1–15 (2017).

11. Brusca, R. C., Moore, W. & Shuster, S. M. Chapter 23: Phylum Arthropoda. in *The Invertebrates. Third Edition* (Sinauer Associates, Sunderland, MA, USA, 2016).

12. Clark, E., Peel, A. D. & Akam, M. Arthropod segmentation. *Development* **146**, dev170480 (2019).

13. Buckley, C. E. & Johnston, D. S. Apical–basal polarity and the control of epithelial form and function. *Nat. Rev. Mol. Cell Biol.* **23**, 559–577 (2022).

14. Classen, A.-K., Anderson, K. I., Marois, E. & Eaton, S. Hexagonal Packing of *Drosophila* Wing Epithelial Cells by the Planar Cell Polarity Pathway. *Dev. Cell* **9**, 805–817 (2005).

1030 15. Gibson, M. C., Patel, A. B., Nagpal, R. & Perrimon, N. The emergence of geometric order in
1031 proliferating metazoan epithelia. *Nature* **442**, 1038–1041 (2006).

1032 16. Farhadifar, R., Röper, J.-C., Aigouy, B., Eaton, S. & Jülicher, F. The influence of cell
1033 mechanics, cell-cell interactions, and proliferation on epithelial packing. *Curr. Biol.* **17**, 2095–
1034 2104 (2007).

1035 17. Bardet, P.-L. *et al.* PTEN controls junction lengthening and stability during cell
1036 rearrangement in epithelial tissue. *Dev. Cell* **25**, 534–546 (2013).

1037 18. Nagpal, R., Patel, A. & Gibson, M. C. Epithelial topology. *BioEssays* **30**, 260–266 (2008).

1038 19. Monier, B., Pélissier-Monier, A., Brand, A. H. & Sanson, B. An actomyosin-based barrier
1039 inhibits cell mixing at compartmental boundaries in Drosophila embryos. *Nature Cell Biol.* **12**,
1040 60–69 (2010).

1041 20. Simone, R. P. & DiNardo, S. Actomyosin contractility and Discs large contribute to
1042 junctional conversion in guiding cell alignment within the Drosophila embryonic epithelium.
1043 *Development* **137**, 1385–1394 (2010).

1044 21. Wright, D. A. & Lawrence, P. A. Regeneration of segment boundaries in Oncopeltus: Cell
1045 lineage. *Dev. Biol.* **85**, 328–333 (1981).

1046 22. Zallen, J. A. & Zallen, R. Cell-pattern disordering during convergent extension in
1047 Drosophila. *J. Phys.: Condens. Matter* **16**, S5073–S5080 (2004).

1048 23. Honda, H. Geometrical Models for Cells in Tissues. *Int. Rev. Cyt.* **81**, 191–248 (1983).

1049 24. Tamada, M. & Zallen, J. A. Square Cell Packing in the Drosophila Embryo through
1050 Spatiotemporally Regulated EGF Receptor Signaling. *Developmental Cell* **35**, 151–161 (2015).

1051 25. Dohle, W., Gerberding, M., Hejnol, A. & Scholtz, G. Cell lineage, segment differentiation,
1052 and gene expression in crustaceans. in *Evolutionary Developmental Biology of Crustacea* (ed.
1053 Scholtz, G.) 95–133 (A.A. Balkema, Lisse, 2004).

1054 26. Gerberding, M. & Scholtz, G. Cell lineage of the midline cells in the amphipod crustacean
1055 Orchestia cavimana (Crustacea, Malacostraca) during formation and separation of the germ
1056 band. *Dev. Genes Evol.* **209**, 91–102 (1999).

1057 27. Gerberding, M., Browne, W. E. & Patel, N. H. Cell lineage analysis of the amphipod
1058 crustacean Parhyale hawaiensis reveals an early restriction of cell fates. *Development* **129**, 5789–
1059 5801 (2002).

1060 28. Scholtz, G. & Dohle, W. Cell lineage and cell fate in crustacean embryos--a comparative
1061 approach. *Int. J. Dev. Biol.* **40**, 211–20 (1996).

1062 29. Browne, W. E., Price, A. L., Gerberding, M. & Patel, N. H. Stages of embryonic
1063 development in the amphipod crustacean Parhyale hawaiensis. *genesis* **42**, 124–149 (2005).

1064 30. Spencer, M. A., Jabeen, Z. & Lubensky, D. K. Vertex stability and topological transitions in
1065 vertex models of foams and epithelia. *Eur. Phys. J. E* **40**, 1–17 (2017).

1066 31. Sun, D. A. & Patel, N. H. The amphipod crustacean Parhyale hawaiensis: An emerging
1067 comparative model of arthropod development, evolution, and regeneration. *Wiley Interdiscip.*
1068 *Rev. Dev. Biol.* **8**, e355 (2019).

1069 32. Lawrence, P. A. *The Making of a Fly: The Genetics of Animal Design*. (Wiley-Blackwell,
1070 New Jersey, USA, 1992).

1071 33. Alwes, F., Hinchen, B. & Extavour, C. G. Patterns of cell lineage, movement, and migration
1072 from germ layer specification to gastrulation in the amphipod crustacean Parhyale hawaiensis.
1073 *Dev. Biol.* **359**, 110–123 (2011).

1074 34. Cislo, D. J. *et al.* Active cell divisions generate fourfold orientationally ordered phase in
1075 living tissue. *Nat. Phys.* **19**, 1201–1210 (2023).

1076 35. Extavour, C. G. The fate of isolated blastomeres with respect to germ cell formation in the
1077 amphipod crustacean Parhyale hawaiensis. *Dev. Biol.* **277**, 387–402 (2005).

1078 36. Chaw, R. C. & Patel, N. H. Independent migration of cell populations in the early
1079 gastrulation of the amphipod crustacean Parhyale hawaiensis. *Dev. Biol.* **371**, 94–109 (2012).

1080 37. Patel, N. H. *et al.* Expression of *engrailed* proteins in arthropods, annelids, and chordates.
1081 *Cell* **58**, 955–968 (1989).

1082 38. Heemskerk, I. & Streichan, S. J. Tissue cartography: compressing bio-image data by
1083 dimensional reduction. *Nat. Methods* **12**, 1139–1142 (2015).

1084 39. Keller, R. E. & Trinkaus, J. P. Rearrangement of enveloping layer cells without disruption of
1085 the epithelial permeability barrier as a factor in Fundulus epiboly. *Dev. Biol.* **120**, 12–24 (1987).

1086 40. Price, A. L., Modrell, M. S., Hannibal, R. L. & Patel, N. H. Mesoderm and ectoderm lineages
1087 in the crustacean Parhyale hawaiensis display intra-germ layer compensation. *Dev. Biol.* **341**,
1088 256–266 (2010).

1089 41. Graner, F. & Glazier, J. A. Simulation of biological cell sorting using a two-dimensional
1090 extended Potts model. *Phys. Rev. Lett.* **69**, 2013–2016 (1992).

1091 42. Holtfreter, J. Tissue Affinity, A Means of Embryonic Morphogenesis. in *Foundations of*
1092 *Experimental Embryology* (eds. Willier, B. H. & Oppenheimer, J. M.) 186–225 (Prentice-Hall,
1093 Englewood Cliffs, N.J., 1939).

1094 43. Swat, M. H. *et al.* Multi-Scale Modeling of Tissues Using CompuCell3D. *Methods Cell Biol.*
1095 **110**, 325–366 (2012).

1096 44. Iijima, N., Sato, K., Kuranaga, E. & Umetsu, D. Differential cell adhesion implemented by
1097 Drosophila Toll corrects local distortions of the anterior-posterior compartment boundary. *Nat.*
1098 *Commun.* **11**, 6320 (2020).

1099 45. Scholtz, G., Patel, N. H. & Dohle, W. Serially homologous engrailed stripes are generated
1100 via different cell lineages in the germ band of amphipod crustaceans (Malacostraca, Peracarida).
1101 *Int. J. Dev. Biol.* **38**, 471–8 (1994).

1102 46. Scholtz, G. The formation, differentiation and segmentation of the post-naupliar germ band
1103 of the amphipod Gammarus pulex L. (Crustacea, Malacostraca, Peracarida). *Proc. R. Soc. Lond.*
1104 *B* **239**, 163–211 (1990).

1105 47. Wolff, C. & Scholtz, G. Cell Lineage, Axis Formation, and the Origin of Germ Layers in the
1106 Amphipod Crustacean Orchestia cavimana. *Dev. Biol.* **250**, 44–58 (2002).

1107 48. Gerberding, M. & Scholtz, G. Neurons and Glia in the Midline of the Higher Crustacean
1108 Orchestia cavimana Are Generated via an Invariant Cell Lineage That Comprises a Median
1109 Neuroblast and Glial Progenitors. *Dev. Biol.* **235**, 397–409 (2001).

1110 49. Fischer, A. H. L., Pabst, T. & Scholtz, G. Germ band differentiation in the stomatopod
1111 Gonodactylaceus falcatus and the origin of the stereotyped cell division pattern in Malacostraca
1112 (Crustacea). *Arthropod Struct. Dev.* **39**, 411–422 (2010).

1113 50. Scholtz, G. & Wolff, C. Cleavage, gastrulation, and germ disc formation of the amphipod
1114 Orchestia cavimana (Crustacea, Malacostraca, Peracarida). *Contrib. Zool.* **71**, 9–28 (2002).

1115 51. Keller, R. *et al.* Mechanisms of convergence and extension by cell intercalation. *Philos.*
1116 *Trans. R. Soc. Lond.* **355**, 897–922 (2000).

1117 52. Karess, R. E. *et al.* The regulatory light chain of nonmuscle myosin is encoded by spaghetti-
1118 squash, a gene required for cytokinesis in Drosophila. *Cell* **65**, 1177–1189 (1991).

1119 53. Landsberg, K. P. *et al.* Increased Cell Bond Tension Governs Cell Sorting at the Drosophila
1120 Anteroposterior Compartment Boundary. *Curr. Biol.* **19**, 1950–1955 (2009).

1121 54. Scarpa, E., Finet, C., Blanchard, G. B. & Sanson, B. Actomyosin-Driven Tension at
1122 Compartmental Boundaries Orients Cell Division Independently of Cell Geometry In Vivo. *Dev*
1123 *Cell* **47**, 727-740.e6 (2018).

1124 55. Jain, A. *et al.* Regionalized tissue fluidization is required for epithelial gap closure during
1125 insect gastrulation. *Nat. Commun.* **11**, 5604 (2020).

1126 56. Martin, A. C. The Physical Mechanisms of Drosophila Gastrulation: Mesoderm and
1127 Endoderm Invagination. *Genetics* **214**, 543–560 (2020).

1128 57. Parzen, E. On Estimation of a Probability Density Function and Mode. *Ann. Math. Stat.* **33**,
1129 1065–1076 (1962).

1130 58. Rosenblatt, M. Remarks on Some Nonparametric Estimates of a Density Function. *Ann.*
1131 *Math. Stat.* **27**, 832–837 (1956).

1132 59. Townes, P. L. & Holtfreter, J. Directed movements and selective adhesion of embryonic
1133 amphibian cells. *J. Exp. Zool.* **128**, 53–120 (1955).

1134 60. García-Bellido, A. Pattern reconstruction by dissociated imaginal disk cells of *Drosophila*
1135 *melanogaster*. *Dev. Biol.* **14**, 278–306 (1966).

1136 61. McMillen, P. & Holley, S. A. Integration of cell–cell and cell–ECM adhesion in vertebrate
1137 morphogenesis. *Curr. Opin. Cell Biol.* **36**, 48–53 (2015).

1138 62. Skamrahl, M. *et al.* Cellular segregation in cocultures is driven by differential adhesion and
1139 contractility on distinct timescales. *Proc. Natl. Acad. Sci.* **120**, e2213186120 (2023).

1140 63. Maitre, J.-L. *et al.* Adhesion Functions in Cell Sorting by Mechanically Coupling the
1141 Cortices of Adhering Cells. *Science* **338**, 253–256 (2012).

1142 64. Bao, M. *et al.* Stem cell-derived synthetic embryos self-assemble by exploiting cadherin
1143 codes and cortical tension. *Nat. Cell Biol.* **24**, 1341–1349 (2022).

1144 65. Steinberg, M. S. Adhesion-guided multicellular assembly: a commentary upon the postulates,
1145 real and imagined, of the differential adhesion hypothesis, with special attention to computer
1146 simulations of cell sorting. *J. Theor. Biol.* **55**, 431–443 (1975).

1147 66. Tepass, U., Godt, D. & Winklbauer, R. Cell sorting in animal development: signalling and
1148 adhesive mechanisms in the formation of tissue boundaries. *Curr. Opin. Genet. Dev.* **12**, 572–
1149 582 (2002).

1150 67. Hogeweg, P. Evolving Mechanisms of Morphogenesis: on the Interplay between Differential
1151 Adhesion and Cell Differentiation. *J. Theor. Biol.* **203**, 317–333 (2000).

1152 68. Blankenship, J. T., Backovic, S. T., Sanny, J. S. P., Weitz, O. & Zallen, J. A. Multicellular
1153 rosette formation links planar cell polarity to tissue morphogenesis. *Dev. Cell* **11**, 459–470
1154 (2006).

1155 69. Jacinto, A. *et al.* Dynamic analysis of actin cable function during Drosophila dorsal closure.
1156 *Curr. Biol.* **12**, 1245–1250 (2002).

1157 70. Martin, P. & Lewis, J. Actin cables and epidermal movement in embryonic wound healing.
1158 *Nature* **360**, 179–183 (1992).

1159 71. Maroudas-Sacks, Y. *et al.* Topological defects in the nematic order of actin fibres as
1160 organization centres of Hydra morphogenesis. *Nat. Phys.* **17**, 251–259 (2021).

1161 72. Calzolari, S., Terriente, J. & Pujades, C. Cell segregation in the vertebrate hindbrain relies on
1162 actomyosin cables located at the interhombomeric boundaries. *EMBO J.* **33**, 686–701 (2014).

1163 73. Saadaoui, M., Rocancourt, D., Roussel, J., Corson, F. & Gros, J. A tensile ring drives tissue
1164 flows to shape the gastrulating amniote embryo. *Science* **367**, 453–458 (2020).

1165 74. Lee, J.-Y. *et al.* Wnt/Frizzled Signaling Controls C. elegans Gastrulation by Activating
1166 Actomyosin Contractility. *Curr. Biol.* **16**, 1986–1997 (2006).

1167 75. Serra, M. *et al.* A mechanochemical model recapitulates distinct vertebrate gastrulation
1168 modes. *Sci. Adv.* **9**, eadh8152 (2023).

1169 76. Lienkamp, S. S. *et al.* Vertebrate kidney tubules elongate using a planar cell polarity-
1170 dependent, rosette-based mechanism of convergent extension. *Nat. Genet.* **44**, 1382–1387
1171 (2012).

1172 77. Gallagher, K. D., Mani, M. & Carthew, R. W. Emergence of a geometric pattern of cell fates
1173 from tissue-scale mechanics in the Drosophila eye. *eLife* **11**, e72806 (2022).

1174 78. Dicko, M. *et al.* Geometry can provide long-range mechanical guidance for embryogenesis.
1175 *PLoS Comput. Biol.* **13**, e1005443 (2017).

1176 79. Guignard, L. *et al.* Contact area–dependent cell communication and the morphological
1177 invariance of ascidian embryogenesis. *Science* **369**, eaar5663 (2020).

1178 80. Royer, C. *et al.* Establishment of a relationship between blastomere geometry and YAP
1179 localisation during compaction. *Development* **147**, dev189449 (2020).

1180 81. Kumar, A. & Shivashankar, G. V. Mechanical Force Alters Morphogenetic Movements and
1181 Segmental Gene Expression Patterns during Drosophila Embryogenesis. *PLoS ONE* **7**, e33089
1182 (2012).

1183 82. Ho, M. W., Matheson, A., Saunders, P. T., Goodwin, B. C. & Smallcombe, A. Ether-induced
1184 segmentation disturbances in Drosophila melanogaster. *Roux's Arch. Dev. Biol.* **196**, 511–521
1185 (1987).

1186 83. Dohle, W. & Scholtz, G. Clonal analysis of the crustacean segment: the discordance between
1187 genealogical and segmental borders. *Development* **104**, 147–160 (1988).

1188 84. Scholtz, G. From a Single Cell to Segmental Structures: Crustacean Embryology. in (Oxford
1189 University Press, 2020).

1190 85. Scholtz, G. Evolution of the nauplius stage in malacostracan crustaceans. *J. Zool. Syst. Evol.*
1191 *Res.* **38**, 175–187 (2000).

1192 86. Gupta, T. & Extavour, C. G. Identification of a putative germ plasm in the amphipod
1193 Parhyale hawaiensis. *EvoDevo* **4**, 34 (2013).

1194 87. Nestorov, P., Battke, F., Levesque, M. P. & Gerberding, M. The Maternal Transcriptome of
1195 the Crustacean Parhyale hawaiensis Is Inherited Asymmetrically to Invariant Cell Lineages of
1196 the Ectoderm and Mesoderm. *PLoS ONE* **8**, e56049 (2013).

1197 88. Scholtz, G. Chapter 24: Cleavage, germ band formation and head segmentation: the ground
1198 pattern of the Euarthropoda. in *Arthropod Relationships* (eds. Fortey, R. A. & Thomas, R. H.)
1199 317–332 (Chapman & Hall, London, UK, 1997).

1200 89. Scholtz, G. & Wolff, C. Chapter 4: Arthropod Embryology: Cleavage and Germ Band
1201 Development. in *Arthropod Biology and Evolution* (ed. Minelli, A.) 63–89 (2013).
1202 doi:10.1007/978-3-642-36160-9_4.

1203 90. Wolff, C. *et al.* Multi-view light-sheet imaging and tracking with the MaMuT software
1204 reveals the cell lineage of a direct developing arthropod limb. *eLife* **7**, e34410 (2018).

1205 91. Kontarakis, Z. & Pavlopoulos, A. Transgenesis in Non-model Organisms: The Case of
1206 Parhyale. in *Hox Genes: Methods and Protocols* vol. 1196 145–181 (Springer, New York, NY,
1207 2014).

1208 92. Riedl, J. *et al.* Lifeact: a versatile marker to visualize F-actin. *Nat. Methods* **5**, 605–607
1209 (2008).

1210 93. Shaner, N. C. *et al.* A bright monomeric green fluorescent protein derived from
1211 Branchiostoma lanceolatum. *Nat. Methods* **10**, 407–409 (2013).

1212 94. Rehm, E. J., Hannibal, R. L., Chaw, R. C., Vargas-Vila, M. & Patel, N. H. Fixation and
1213 dissection of Parhyale hawaiensis embryos. *Cold Spring Harb. Protoc.* **2009**, pdb.prot5127
1214 (2009).

1215 95. Kiehart, D. P. & Feghali, R. Cytoplasmic myosin from Drosophila melanogaster. *J. Cell Biol.*
1216 **103**, 1517–1525 (1986).

1217 96. Tomer, R., Khairy, K., Amat, F. & Keller, P. J. Quantitative high-speed imaging of entire
1218 developing embryos with simultaneous multiview light-sheet microscopy. *Nat. Methods* **9**, 755–
1219 763 (2012).

1220 97. Pietzsch, T., Saalfeld, S., Preibisch, S. & Tomancak, P. BigDataViewer: visualization and
1221 processing for large image data sets. *Nat. Methods* **12**, 481–483 (2015).

1222 98. Preibisch, S., Saalfeld, S., Schindelin, J. & Tomancak, P. Software for bead-based
1223 registration of selective plane illumination microscopy data. *Nat. Methods* **7**, 418–419 (2010).

1224 99. Preibisch, S. *et al.* Efficient Bayesian-based multiview deconvolution. *Nat. Methods* **11**, 645–
1225 648 (2014).

1226 100. Schindelin, J. *et al.* Fiji: an open-source platform for biological-image analysis. *Nat.*
1227 *Methods* **9**, 676–82 (2012).

1228 101. Berg, S. *et al.* ilastik: interactive machine learning for (bio)image analysis. *Nature Methods*
1229 **16**, 1226–1232 (2019).

1230 102. Heemskerk, I. & Streichan, S. J. Tissue cartography: compressing bio-image data by
1231 dimensional reductio n. *Nature Methods* **12**, 1139–1142 (2015).

1232 103. Etournay, R. *et al.* TissueMiner: A multiscale analysis toolkit to quantify how cellular
1233 processes create tissue dynamics. *eLife* **5**, e14334 (2016).

1234 104. Stringer, C. & Pachitariu, M. Cellpose3: one-click image restoration for improved cellular
1235 segmentation. *bioRxiv* 2024.02.10.579780 (2024) doi:10.1101/2024.02.10.579780.

1236 105. Aigouy, B., Umetsu, D. & Eaton, S. Segmentation and Quantitative Analysis of Epithelial
1237 Tissues. in *Methods in Molecular Biology: Drosophila Methods and Protocols* (ed. Dahlmann,
1238 C.) vol. 1478 227–239 (Springer New York, New York, NY, 2016).

1239